CESIUM HYDROGEN SULPHATE AND CESIUM DIHYDROGEN PHOSPHATE BASED SOLID COMPOSITE ELECTROLYTE FOR FUEL CELL APPLICATION

by

Sivapregasen Naidoo

CESIUM HYDROGEN SULPHATE AND CESIUM DIHYDROGEN PHOSPHATE BASED SOLID COMPOSITE ELECTROLYTE FOR FUEL CELL APPLICATION

by

Sivapregasen Naidoo

A thesis submitted in fulfilment of the requirements for the degree of Magister Scientiae in Chemistry in the Department of Chemistry, University of the Western Cape.

Supervisor: Professor Vladimir Linkov
Co-Supervisor: Doctor Guntars Vaivars

I would like to thank my supervisor, Vladimir Linkov and Co-supervisor, Guntars Vaivars for the assistance and expertise offered during the research. I would also like to offer a special thank you to David Kok (Fine Chemicals-Aspen Pharmaceuticals), Thaven Naidoo (Caltex), Thesigan Naidoo (Cape-Tech), Vaneshree Naidoo, Paulos Mahlangu and Michael Crooke for their time and analytical support.

I was privileged to be part of multi-skilled laboratory personnel who were always keen to assist me when necessary.

Finally, the unconditional family support which, I certainly would not have being able to have done without.

ABSTRACT

A new high temperature solid electrolyte composite was developed, with $CsHSO_4$ and CsH_2PO_4 as the proton conducting material in composition with PTFE and SiO_2 to enhance the solid electrolyte composites mechanical strength and conductivity. Conductivity measurements for $CsHSO_4$ and CsH_2PO_4 and composites thereof, in temperature ranges 0 to 180 ^oC and 0 to 250 ^oC respectively, were carried out. The composites with different concentrations PTFE and silica were tested for stability in a hydrogen atmosphere and different degrees of humidity. The $CsHSO_4$ was seen to exhibit a super protonic phase change at temperatures between 132 – 140 ^oC and CsH_2PO_4 around 230 ^oC. The presence of the PTFE proved to be a stabilizing factor in the reduction of water re-adsorption once the membrane had been dried during thermal conductivity analysis. According to supporting data in the literature it has been found that composites including silica could be influenced by the hydrophilicity and specific surface area of the silica. In the composite system employed it was shown by impedance analysis the presence of two semi-circles in the Nyquist representation for the enhanced conductivity due the presence of silica. The presence of point defects formed at the interface between ionic salt and silica could result in the enhanced conductivity.

TABLE OF CONTENTS PAGE

Cesium Hydrogen Sulphate and Cesium Dihydrogen Phosphate Based Solid Composite Electrolyte for Fuel Cell Application

TABLE OF CONTENTS PAGE

LIST OF FIGURES Page

$CsHSO_4$ Cesium Hydrogen Sulphate

CsH_2PO_4 Cesium Dihydrogen Phosphate

SiO_2 Silicon Dioxide (Silica)

PTFE Polytetrafluoroethylene

MEA Membrane Electrode Assembly

CBES Catalyst, Binder and Electrolyte Solution

IR Infrared Spectroscopy

SEM Scanning Electron Microscopy

TGA Thermal Gravimetric Analysis

XRD X-Ray Diffraction

PEMFC Proton Exchange Membrane Fuel Cell

FRA Frequency Response Analysis

H Hydrogen

D Deuterium

NMR Nuclear Magnetic Resonance

DSC Differential Scanning Calometery

CsI Cesium Iodide

$CsDSO_4$ Cesium Deuterium Sulphate

MCFC Molten Carbonate Fuel Cell

AFC Bacon Molten Alkali Electrolyte Fuel Cell

KE Kinetic Energy

Pt/C Platinum on Carbon

BET The Brunauer-Emmett-Teller equation

CHAPTER 1

1. MOTIVATION AND OBJECTIVES

1.1 BACKGROUND

Researchers throughout the world are seeking effective proton conducting membranes for fuel cell application. Proton conducting membranes form an integral part of the PEMFC. A major investment of resources has been made to obtain a proton conducting membrane, which could be incorporated in mobile power sources.

Currently the major developments in fuel cell technology using hydrogen or methanol are based on perfluorinated and sulfonated solid polymer electrolytes. The fact that fuel cells run on hydrogen or hydrogen carriers points to the link between fuel cells and the so-called hydrogen economy. This is a significant observation since hydrogen fuel technology is a sustainable technology and may be one of the best long-term solutions to the energy problem. These solid electrolytes offer advantages over classical liquid electrolytes such as sulphuric acid. These advantages include reduced methanol fuel crossover and higher power densities. Sulphonic acid insertion into solid polymer membrane is currently employed and is commercially referred to as Nafion®. This membrane is very popular when used as a low temperature proton conducting polymer membrane with thickness between 25 and 175 μm. This membrane is a good proton conductor and is the preferred membrane for both hydrogen and direct methanol fuel cells (DMFC).

However, it has some problems that limit the manner in which it can be successfully used in fuel cells. The methanol fuel crossover reduces the cell potential difference; the Nafion

is generally very expensive and the membrane operates below 100°C as the water content diminishes with temperatures greater than 100 ^{o}C.

The operating temperature of a fuel cell is an important characteristic. A high temperature fuel cell may be very efficient in an application where both its electricity and heat can be used. Heat however is not desired in applications such as lap top power supplies and motor vehicles, and therefore low temperature fuel cells such as the PEMFC are a better option as power sources in fuel cell vehicles. A membrane with higher operating temperatures, and higher mechanical strength would be useful for fuel cell applications. A number of researchers are therefore experimenting with ceramic inorganic membranes [1-5].

1.2 EXISTING PROBLEMS

- Nafion® is very expensive and has a negative influence on pricing resulting in high cost fuel cells not affordable to the public.
- Most membranes currently used in PEMFCs and DMFCs were not designed to operate at high temperatures where high temperature fuel cells have the ability to reform some hydrocarbon fuels directly.
- The high methanol permeability through the membrane resulting in catalyst poisoning and reduced cell potential.
- Low temperature designed membranes such as Nafion® dehydrates as the temperature nears and exceeds 100°C.

1.3 OBJECTIVES

- To produce membranes of $CsHSO_4$ and CsH_2PO_4 with high conductivity to operate at temperatures exceeding 100^oC.
- To test the conductivity of the membrane with thermal dependence conductivity using the FRA technique.
- To determine the effectiveness of different precursors in the manufacture of the proton conductor, cesium hydrogen sulphate, viz cesium sulphate (Cs_2SO_4) and cesium carbonate (Cs_2CO_3).
- To test and compare the conductivity of each method of manufacture when using different precursors.
- To characterize the formed membranes by SEM, IR, TGA and XRD analysis.
- To reinforce the membranes to withstand heat, prevent moisture from affecting the conductivity and reduce degradation by pH changes, and enhancing the physical and mechanical strength of the membrane.
- To test the conductivity of the reinforced composite membrane and compare to that of the membrane without the insulator, PTFE.
- To subject the composite membrane to stability and robust testing to determine the pH changes and dissolution rate by altering temperature and mechanical variables such as stirring rates.

1.4 RESEARCH STRUCTURE

Composite formation was used to stabilize the inorganic solid acid electrolyte, cesium hydrogen sulphate membrane due to the solubility and degradation the membrane undergoes once the fuel is brought in contact with the membrane, which adversely affects the conductivity. The additive material of choice to prepare these composites will be PTFE, due to its resistance to chemical attack, and silica to enhance conductivity and surface area. Different types of composite membranes will be developed with varying volume fractions of the component concentration and using different precursors.

1.5 STRUCTURE OF THESIS

- Chapter 2: Introduction to fuel cells and literature review. Presents a theoretical overview, of the research.
- Chapter 3: Experimental. Outlines the methods employed and the principles supporting the characterization techniques when producing and testing the membranes.
- Chapter 4: Pure Cesium Hydrogen Sulphate Salt. Presents the experimental results and interpretation of the data obtained.
- Chapter 5: Cesium Hydrogen Sulphate in Composite formation. Presents the experimental results and interpretation of the data obtained.
- Chapter 6: Cesium Dihydrogen Phosphate in Composite formation. Presents the experimental results and interpretation of the data obtained.
- Chapter 7: Summary. Summary of the main findings and future work.

CHAPTER 2

2. INTRODUCTION

The fuel cell was invented by Sir William Grove in 1839, while trying to reverse the process of splitting water using electricity (electrolysis). The first fuel cells capable of producing significant power were only produced in 1959 and were used in demonstrations to power welding machines and tractors. NASA used the fuel cells in the space program and the fuel cell is still of interest to NASA since much research is being carried out to date. Fuel cells are undeniably the more effective source of power for transportation. They also have obvious advantages such as high efficiency, clean operation and low power densities.

Fuel cells use a combination of hydrogen and oxygen (as fuel) to produce electricity, water and heat. Similarly to a battery, a fuel cell has a positive electrode (anode) and a negative electrode (cathode) between which the electricity moves and a solution (electrolyte) that carries the ions between the electrodes. This is where the similarity ends however, because a battery consumes one of the electrodes while producing electricity. A fuel cell has the unique ability to supply fuel to the process at a constant and continuous rate. Hydrogen or methanol is fed at the positive electrode end and oxygen at the negative electrode end. In a fuel cell the electrolyte allows for the transport of protons. The electrolyte does not allow electrons to pass through it and are subsequently directed through an electric circuit to reach the negative end where they rejoin the proton. The oxygen at the negative end electrode combines with the hydrogen to form water as the end product.

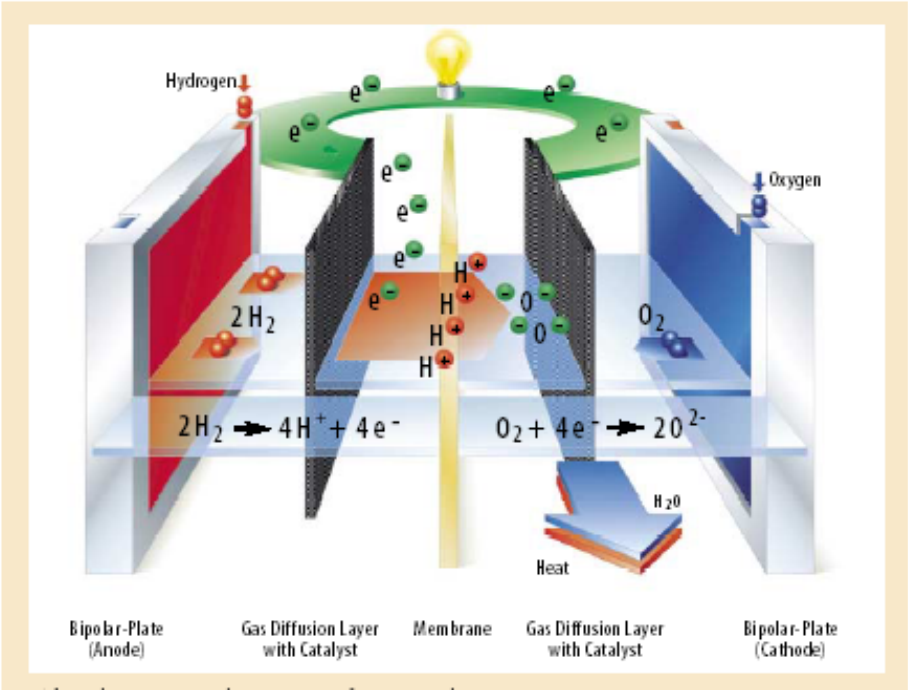

Figure 2.1: An illustration of a working fuel cell.

Fuel cells function using different electrolytes to transport ions. The nature and composition of electrolyte used will determine the operating temperature of the fuel cell and its susceptibility to impurities in the fuel. Normally the higher the operating temperature of the fuel cell the longer it takes to reach its function optimum temperature but is more tolerant of impurity presence in the fuel. Some of the higher operating fuel cell temperatures are those with the solid oxide and the molten carbonate electrolytes. Here, the use of either a solid ceramic or a liquid carbonate salt as the electrolyte, carries hydrogen ions over to the waiting oxygen. The high temperatures (600-1000°C) allow the oxygen and hydrogen, along with impurities such as carbon monoxide, to combine to form water and carbon dioxide as byproducts. The high temperature type fuel cells do not necessarily have to be fed only hydrogen or methanol as fuel sources as natural gas or petroleum which are broken down into hydrogen and carbon monoxide by the heat and

catalyst at the anode, can also be used. The phosphoric acid electrolyte contained in fuel cells which operate at 150-200°C needs a fuel supply of hydrogen which does not have to be as pure as that used for the polymer electrolyte fuel cell.

2.2 LITERATURE REVIEW

2.2.1 Factors Affecting Electrolyte Selection

The electrolyte should ensure high proton conductivity. The water drag, if present, has to be minimal or preferably non-existent. When methanol is incorporated at the anode a crossover occurs adversely affecting the cathode and there is a resulting drop in the potential of the cell. Thus a membrane is required with reduced or non-existing crossover levels. The electrode that also incorporates the polymer or electrolyte in its electrode structure has to have gas permeability capability, thereby allowing the resulting gases to leave the reaction site on the electrode. The electrolyte has to offer a favourable environment for chemical reaction to take place. Under harsh conditions of temperature increases and pressure changes the electrolyte requires chemical and physical stability. Due to the physical contact, portability, pH and flow rate amongst other factors, which the electrolyte has to endure, requires electrolytes with tough mechanical properties. Cost is often the deciding factor when large-scale production for commercialization is contemplated.

2.2.2 Intermediate Temperature-High Temperature Fuel Cells

CsH_2PO_4–based composites like the solid oxide fuel cells (SOFC) can be classified as intermediate temperature types operating between 100 and 300^oC. The intermediate temperature fuel cells have the advantages of effective use of excess energy in the form of heat, increased catalytic activity with less expensive catalysts, and reduction in crossover levels. The high operating temperature reduces the chances of CO poisoning with out the need for fuel cleansing features reducing the complexity of the system.

The solid acid fuel cells can be operated without water to transport the protons across the membrane and unlike the polymer electrolyte membrane fuel cell, solid acid electrolyte fuel cell membranes are less corrosive and able to utilize high energy density alcohol fuels such as methanol since they are impermeable to methanol. The melting point of CsH_2PO_4 is relatively quite high, at 345^oC [11].

2.2.3 Nafion-zirconium phosphate

The relative humidity needs to be in the region of 90% for the effective operation of the high temperature proton conducting membrane. To maintain the relative humidity the water vapor pressure required is sustained by increasing the pressure of the fuel cell system [1]. The distribution and particle size of the fine sulphated zirconia employed, are factors affecting the performance of the membrane composed of recast Nafion [1]. The improved performance of the Nafion zirconium phosphate membrane as compared to the Nafion/sulphated zirconia is largely influenced by the distribution of the inorganic phase within the Nafion membrane. Impregnation of the zirconium phosphate forms a continuous structure connecting the ion-cluster domains of the Nafion. This allows for

the hydration of the entire membrane with enhanced conductivity. The surface acidity of some inorganic compounds may increase proton conductivity [2,3].

Activation Energy values indicate a small difference between Nafion and composite Nafion/zirconium phosphate membranes probably related to the mechanism for proton conductivity and conductivity properties [4].

The MEA can be characterized using cell potential vs. current density plots

$$E = E_0 - b \log(i) - R_i \quad \text{..... Equation 2.1}$$

$$E_0 = E_r + b \log(i_0) \quad \text{..... Equation 2.2}$$

In equation 2.1 and 2.2, the parameter E_0 is a fitting parameter which is related to the open circuit potential, E_r is the reversible cell potential (Nernst Equation), i_0 and b are the Tafel parameters for oxygen reduction and R represents the resistance which causes a linear variation of E with i. Resistance R is largely influenced by the ionic resistance of the electrolyte, from the mass transport resistance existing in the electrodes, and their contact with the current collectors [5].

E_0 is lower for recast Nafion membrane as it is much thinner and methanol crossover could be easier facilitated. The open circuit voltage decreases, which is directly affected by E_0 thus methanol crossover. Impregnation of Nafion with zirconium phosphate improves the E_0 value largely due to reducing the crossover effect. The R value decreases at high temperatures indicating the influence of the water retention properties of zirconium phosphate. The electrode electro-kinetics is enhanced by the water retention properties of the ion-conducting phase [4].

2.2.4 Pure Cesium Dihydrogen Phosphate and Cesium Dihydrogen Phosphate-Silica Composite

2.2.4.1 Pure CsH_2PO_4

The ionic conductivity of CsH_2PO_4 is controlled by the water content [6,7]. Superionic phase transitions from monoclinic to cubic CsH_2PO_4 have been recorded occurring around 230 to 231°C. This transition is reversible and occurs in humid conditions. Under dry conditions and above 230°C, formation of dimer and trimer products etc., which coat the polymer surface with a thin solid layer, gradually lowers the conductivity. For controlled humidified conditions the phase transition is accompanied by changes in the crystal symmetry from monoclinic to cubic and some interstitial proton sites become structurally similar to the normal proton sites. With the number of proton sites increasing relative to the number of protons, the protons are scattered chaotically between the proton sites. The CsH_2PO_4 superprotonic conduction is a combination of the dynamic phase occurring in tandem with ordered-transition phases [6].

2.2.4.2 Mechanisms of Proton Conduction at the Interface for CsH_2PO_4/SiO_2–Based Composites

At the ionic salt and oxide interface an increase in conduction has been noted. This was shown using impedance analysis for CsH_2PO_4 composites. The conduction at the interface can be described as the enhancement of ionic conduction because of the surface interaction between the ionic conductor and insulator heterojunction. Different models for ionic conduction are proposed, namely, space charge model, defect-induced order-disorder phase transitions (or defect-induced sublattice melting) and formation of a structurally disordered phase.

2.2.4.3 Space Charge Model for Conductivity

Proton movement contributing to ion conductivity proceeds by two interactions as follows: Firstly, an attractive interaction, where the diffusion of cations from their regular sites to the surface of the insulator (dispersoid) stabilized by sorption, thus, increasing the vacancy concentration at the interface. And secondly, repulsive interactions, which occur when the cation accumulates in the interstitial site area driven by the insulator. The two interactions contribute to defect formation at the interface, which can improve the interfacial ion conductivity of the ionic conductor/insulator composites [8].

2.2.4.4 Defect-Induced Order-Disorder Phase Transitions Model

Order-disorder phase transition responsible for ionic conduction is stimulated by the defects in the interface region. The critical temperature of the order-disorder phase transition is thought to be lowered by the defects occurring at the interface. Once the temperature drops below the super-ionic phase transition, there is an increase in ionic conductivity [9].

2.2.4.5 Formation of a Structurally Disordered Phase Model eg. For ($CsHSO_4$-SiO_2)

The conductivity of $CsHSO_4$-SiO_2, among other ionic salt composites, is governed by the ionic salt and oxide structural make up at the interface region. The stability of the interface region is dependent on the adhesion energy between ionic salt and oxide. Also the conductivity is dependant on the physical properties of the interface region between the ionic salts and the oxides, which essentially differ from the properties of individual compounds. It was also pointed out that the structural reconstruction or formation of the meta-stable interface occurs due to strong adhesion. The resulting interface from the

ionic salt spreading over the oxide particle will be structurally disordered accounting for the high conductivity.

Application of the mechanisms mentioned above to the CsH_2PO_4/SiO_2 composite,

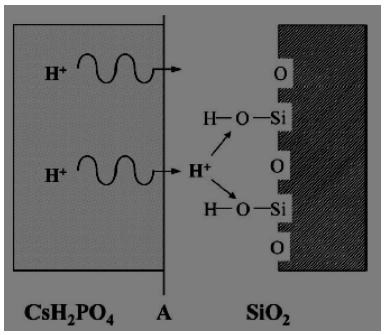

Fig. 2.2: A schematic representation for the interaction between silica with proton.

The surface of the hydrophilic silica is covered by polarized surface-like OH.

The space charge model promotes the attractive interaction concept for this system. The theoretical understanding expects that protons in CsH_2PO_4 move or diffuse to the interface to be stabilized by sorption on SiO_2 as represented in fig. 2.2.

2.2.5 Influence of Thermal and Mechanical Treatment and of Water on Structural Phase Transitions in $CsHSO_4$

$CsHSO_4$ experiences two, phase transitions at temperatures of 318 and 417K. At 417K a high proton conductivity state is reached at a value of $10^{-2}\Omega^{-1}cm^{-1}$. This super-ionic property makes $CsHSO_4$ a favourable component in electrochemical devices such as batteries, fuel cells, displays and super-capacitors. $CsHSO_4$ can also be used as a model to understand the mechanism of proton conductivity in “dry” proton conductors where “wet” and “ion jump” type conduction takes place.

2.2.6 Various Phases and Structures of $CsHSO_4$

$CsHSO_4$ has 3 phases. Phase I is the room temperature structure consisting of a hexagonal array of cesium ions stacked along a bent direction. Zigzag chains of hydrogen bonded HSO_4^- ions are perpendicular to the loose packed Cs^+ ion plane and imprison the Cs^+ ions.

The structure is an intermediate between the non-protonic glasrite structure and the ferroelectric CsH_2PO_4 structure with two different types of hydrogen-bonded chains surrounding the Cs^+ cations. X-ray diffraction shows the phase I structure, which is confirmed by infrared and Raman spectra, particularly the statistical distribution of protons between two potential minima of the OH…O hydrogen bonded chains. There are two first order phase transitions one observed at approximately 318K (I→II) and the other at 417K (II→III). Due to the weakening of the hydrogen bonds and a structural disorder of the anions, the I→II transition has been interpreted on the basis of spectral vibration analysis where a conversion of infinite chains into cyclic dimers occurs. For the superionic phase III there is a further weakening of the hydrogen bonds and an increasing level of disorder. There is also evidence of rapid re-orientation of HSO_4^- species and translation disorder of Cs^+ ions. The high proton mobility was observed by H and D NMR, as well as quasi-elastic neutron scattering [6-14].

Upon cooling, metastable phases (III→II→I) occur, with long annealing below 280K being required to reach the phase I stage. More importantly, the kinetics is largely influenced by the presence of water traces. Samples prepared by slowly evaporating solutions of Cs_2SO_4 and H_2SO_4 to produce small crystals (0.5 to 1 mm), do not undergo

phase transitions when stored in a sealed container. However complex DSC traces are observed for the temperature range 315-380K. This is supported by the measured enthalpy values (ΔH) for the I→II transition which varies reversibly between 4.8 and 14.4 kJ/mol being dependant on the "defect" concentration, while the II→III (II↔III) phase transition ΔH value yields approximately 14.4 or 29.2 kJ/mol. The stretching intensity of the S-O and S-OH bands is directly influenced by the grinding force during the sample preparation and is not affected by the time factor. For the CsI pellet the pressure must be applied for a few hours before the 998 cm^{-1} band disappears but does not vary with time thereafter. Weak and strongly ground samples show different spectra. The Raman spectrum shows typical cyclic dimer occurrence as in phases II and I. Thus, $CsHSO_4$ at room temperature can be structurally modified by mechanical treatment which converts the infinite chains of HSO_4^- ions into cyclic dimers. The applied pressure also referred to as the mechanical treatment, is responsible for the chain/dimer ratio.

Structure of $CsHSO_4$

When equivalent molar amounts of Cs_2SO_4 and H_2SO_4 in an aqueous solution are heated to 333K and allowed to cool to room temperature, colourless crystals are formed depicting a twin structure. Using a three dimensional Patterson map the positions of the Cs and S were found **[13]**.

A map of residual electron density showed an anomaly reflected near the Cs atom of maximum of 1.6 eA^{-3}. Cs and SO_4 lie on the mirror planes y = ¼ and ¾. There are one-dimensional chains of hydrogen bonds along the *b* axis. In the Para-electric phase $CsHSO_4$ resembles CsH_2PO_4 the only difference is the extra H atom which combines O (1) and O (2^{11}) [14]. There is also evidence of a disordered H atom. Below room

temperature a phase transition could be responsible for the conversion to the ordered phase.

When using vibrational spectra, the external modes obey the selection rules where Z = 2 for the C_{2h} factor group. Thus the average symmetry of the crystal is seen in the same way as by X-rays [16]. For the Raman spectra seven out of the nine Raman active lattice bands below 300 cm^{-1}, were observed. In the low temperature powder spectrum seven Raman bands were also observed.

The lattice bands can be assigned approximately in terms of the rotational (R') and translational (T') vibrations of the HSO_4^- ion (250-100cm^{-1}) and translational modes (T') of the Cs^+ cation (below 80 cm^{-1}).

Internal vibrations do not indicate the center of symmetry or the SO_4 mirror plane. In the skeletal bending region (650-350 cm^{-1}) there are more bands than expected with coinciding frequencies [17,18]. The spectral pattern for S-O stretching is similar to that of other alkali hydrogen sulphates which do not contain symmetrical hydrogen bonds [19]; the particularly strong Raman bands near 990 and 860 cm^{-1} could be due to a S-O proton acceptor and a S-OH proton donor group, respectively. For the OH---O hydrogen bond the νOH mode is responsible for broad ABC bands.

These bands are characteristic of strong hydrogen bonds and their center of gravity at 2400 cm^{-1} is in agreement with O---O distances of 2.57A [18]. When $CsHSO_4$ is heated to 350K, I→II transition takes place. The νS-O frequency at 998 cm^{-1} shifts suddenly to 1024 cm^{-1} and the νS-OH band broadens and it's frequency decreases to 850 cm^{-1}. As mentioned before, this also reflects the conversion of infinite chains to cyclic dimers containing a weaker hydrogen bond.

The νOH band shift towards higher wave numbers also indicates the weakening of the hydrogen bonds. The Raman bands for R'_{HSO4}^{-} and T'_{HSO4}^{-} broaden considerably, in the lattice region, showing the anions to be in a structural disorder [17, 18].

Further broadening of the super-ionic phase III bands due to internal vibrations indicates an increasing structural disorder. More significantly, is the further loosening of the hydrogen bonds supported by the upward movement or shift of the νOH band. This is also indicated by the increased difference between νS-OH and νS-O frequencies. From an analytical point of view, the most obvious and striking change is observed in the lattice region where all the external mode bands collapse into a broad band near the Rayleigh line as for H_3OClO_4. This is also evident in a highly disordered (plastic) crystal, indicating a rapid re-orientation of the HSO_4^- ions on their sites and translational disorder of cesium with this being an identical characteristic in other cationic superconductors [20, 21, and 22]. Thus the proton transfer in phase III is only partially involved in the total ionic motion but more importantly the Cs^+ ions are major contributors to the conduction process [23]. This is in agreement with the super-ionic properties of parent non-proton conducting sulphates and work done using D NMR on $CsDSO_4$.

This view is supported by deuterium studies, which shows the conductivity varying only in phase III where the activation energy (E_a) is 0.32 and 0.27 eV for $CsHSO_4$ and $CsDSO_4$ respectively. Due to a resulting 200 fold decrease in conductivity when hydrogen is substituted by deuterium, phases, II and I low temperature conductivity should essentially be protonic. The conductivity mechanism strongly supports a proton tunneling stage. A possible explanation for the Cs^+ ion contribution to the conductivity is

the transition from the super-ionic to the low temperature phase being accompanied by a 500 times drop in conductivity associated with a difference in the electrostatic repulsion between cations. The sulphate orientation is associated with the restricted motion of the larger cations preventing local motion of the protons. This property is evidence of the large pressure effect on super-ionic properties [24, 25, 26, 27].

2.2.7 Composite Protonic Solid Electrolytes in the $CsHSO_4$-SiO_2 System

A compounds conductivity mechanism which depends on H_3O^+ ions, relies on the H_2O content. This was the basis for the addition of a heterogeneous component with the intention to increase the proton conductivity of $CsHSO_4$. Initial heating shows an increase in conductivity but this is due to the loss of water on drying. However the completion of three heating and cooling cycles heating to 485K and cooling to 300K, produced reproducible conductivity results. The composite investigated was (1-x) $CsHSO_4$-xSiO where x, the mole ratio of heterogeneous component SiO_2, varied from 0 to 0,8. The addition of the SiO_2 does not increase the conductivity of the composite membrane if the initial powder was not heated near to its melting point temperature. Shown here, the conductivity is largely influenced by the mole ratio of SiO_2. Increasing the SiO_2 mole fraction in the proton conducting membrane composite increases the ion conductivity in the super-ionic phase at low temperatures. Increasing the SiO_2 concentration of the composite to greater than 20% shows a significant increase in the conductivity. This concentration dependency supports the percolation theory that conducting pathways formed by highly conducting interfaces. This high conductivity at

low temperatures can be ascribed to water adsorbed on the surfaces of the highly dispersed SiO_2. To eliminate this contribution to the conductivity tests were carried out where the partial pressure of water was decreased to 10^{-1} Pascals. There was no effect on the conductivity at low and high temperatures, thus supporting the conduction mechanism as structural protons rather than hydronium ions although it is a hydrated compound [30].

In the high temperature region (380-483K) composites containing SiO_2 with concentrations in the region of 10-60%, have higher conductivities than pure $CsHSO_4$. This could be the stabilization of the molten $CsHSO_4$ on the surface of the highly dispersed SiO_2. Based on the conductor-insulator type percolation where the insulator does not possess protons or any conductive properties, high SiO_2 concentrations in the region of 60-80% result in a decrease in conductivity [31, 32].

Heterogeneous doping component addition of the composite with SiO_2 affects not only the conductivity properties but also the temperature at which the super-ionic phase takes place. Differential thermal analysis (DTA) suggests two intensive peaks. The first DTA peak appears at 485K for pure $CsHSO_4$, and the other at 414K representing the process of crystallization and phase transition respectively. Reported data supports these results where the phase transition enthalpy is approximately 5.5 kJ/mol and the crystallization enthalpy is approximately 9.5kJ/mol [30, 33]. As the amount of SiO_2 increases the temperature and enthalpy of crystallization (melting) and phase transition, decrease. When the SiO_2 concentration is greater than 50% the thermal effects relating to the phase transition of crystallization (melting) decrease one order of magnitude as compared to

pure $CsHSO_4$. This depicts the favourable influence heterogeneous doping has on the thermodynamic parameters of the $CsHSO_4$ as an ionic conductor. XRD analysis of composite $CsHSO_4$-SiO_2 at varying concentrations of SiO_2, after the composite was heated to 483K, showed a decrease in intensity with the peaks becoming broader notably in composites containing more than 50% SiO_2. All reflections correspond to the structure of low temperature β-phase of $CsHSO_4$. In composites with SiO_2 content greater than 50% in the $CsHSO_4$ membrane, the XRD patterns show a weak halo appearing in addition to the crystalline phase. When the SiO_2 concentration is greater than 30% in the composite, an additional reflection at $2\theta = 24.8^o$ appears. The additional reflection corresponds to the super-ionic α-phase of $CsHSO_4$ and lacks the X-ray diffraction patterns of the β-phase [47, 48].

Possible explanations for the sharp increase in the composite conductivity include the diminishing of grain size and the formation of a space-charge region at the interface. For low concentrations of SiO_2; firstly, the presence of the amorphous $CsHSO_4$ phase on the highly dispersed SiO_2 surface relating to SiO_2 concentrations less than 50% and secondly the above in combination with the possible stabilization of $CsHSO_4$ with PTFE could be responsible for the sharp increase in the composite conductivity [30].

2.2.8 Silicon Dioxide (silica) SiO_2

Occurring in the earths crust as the second most abundant element, silicon has a variety of forms including sand, quartz and flint and as silicates in rocks and clays. Silica occurs in different crystalline forms, each containing silicon atoms bonded tetrahedrally to four oxygen atoms by means of single Si-O bonds. Silicon dioxide (silica) is different to carbon dioxide in its structure and silicon does not readily form multiple bonds. Silica

has three crystalline forms, namely quartz, tridymite, and cristobalite each possessing a high and low structural modification. Quartz is the most thermodynamically stable. This is further supported by the high activation energy requirements for the movement of atoms in solids. The structure of the crystobalite is similar to the diamond structure where silicon atoms replace the carbon atoms with one oxygen atom midway between two silicon atoms. For the quartz and tridymite, spiral structures are present with optical isomers forming right and left handed spirals. The three forms of silica have covalent bonds extending in three dimensions, resulting in gigantic molecules that have high melting points. The empirical formula corresponds to SiO_2 due to each silicon atom being shared equally by two oxygen atoms. Glass is formed when molten silica is allowed to cool. The chains are randomly orientated with sheets and three-dimensional networks of SiO_4 groups [30].

2.2.9 PTFE(Teflon) in Composites

Due its low surface energy, PTFE is not wettable and does not directly adhere to any solid. PTFE can thus be characterized as both hydrophobic and oleophobic.

PTFE (Teflon) composites and Percolation [10]

The conductivity of PTFE is of the order of $10^{-10}Scm^{-1}$. The conductivity of the composite is clearly lower than that of the pure ion conducting substance as the composite is dominated by grain boundary contribution i.e. ion movement across boundaries of neighboring conducting substance particles. For PTFE in $LiSn_2P_3O_{12}$ composite a percolation expression $\sigma=\sigma_0(\nu-\nu_c)^t$, for $\nu\geq \nu_c$; where σ_0 is a pre-exponential factor, ν_c is the critical volume fraction of the conducting substance $LiSn_2P_3O_{12}$, *t* is an exponent. For a 3-dimensional percolation system the t value is approximately 2, slightly

lower than the exponent. The critical volume fraction is nearly the same as the conducting substance area fraction of approximately 0,3. For a random distribution of conducting particles (ν_c=0.15-0.17) higher values are predicted for the critical volume fraction. This is explained in the aggregation process to give extended clusters formed in isolation the form of an intermediate stage. To lower the critical volume fraction the composite could be prepared by a different procedure that disperses of the ceramic particles.

2.2.9.1 The Percolation Theory

The percolation theory was used to prepare composites with varying electrical properties, to be more water proof without compromising the composites ability to be a superior high temperature ionic conductor. Percolation theory is only applied when the conductivity of the lower conducting phase is zero. The conductivity of the composite medium near the transition from metal to insulating phase, can be explained with an equation obtained from the percolation theory. Although the percolation theory has been developed employing regular lattices it can also be used to explain the conductivity characteristics of graphite-polymer mixtures [28].

General Effective Medium Equation

The combination of the Bruggeman effective media and the percolation theories results in the general effective media equation. This equation explains the actual results obtained experimentally from composite media electrical impedance testing. As in the percolation theory, the volume fraction and the exponent *t* are two parameters which characterize the shape, spatial distribution and interconnectivity of the conducting particles [28].

Critical Volume Fraction

The critical volume fraction varies between 0.1 and 0.6 in composite media [28]. Ionic resistance decreases as a function of the volume fraction of the higher conducting phase when the average number of contacts per grain is about 1 and stops decreasing when the average number of contacts per grain is about 2 [29]. A critical percolation volume fraction "basic" value could be in the region of 0.16, refer to Table 2.1

Table 2.1: Critical Parameters for Bond Site Percolation on a Variety of Lattices

Lattice	P_{cb}	P_{cs}	Coordination, Z	Filling factor, V	ZP_{cb}	$vP_{cs}=\phi$
Fcc	0.119	0.198	12	0.7405	1.43	0.147
Bcc	0.179	0.245	8	0.6802	1.43	0.167
Sc	0.247	0.311	6	0.5236	1.48	0.163
Diamond	0.388	0.428	4	0.3401	1.55	0.146
rcp		0.27		0.6		0.162
Average					1.5±0.1	0.16±0.02

2.3 PRINCIPLES OF MEA PREPARATION

The criteria for the formation of effective electrode structures is (1) the presence of electrolyte over the electrode with access to reactant gases and avoiding drying or drowning, (2) possessing a high surface area for the reaction to take place, (3) having an invariant electrolyte and (4) analysis of the cells using I/V curves. Early fuel cell

electrodes were classified as porous metal sintered electrodes and the gas diffusion or polytetrafluoroethylene (PTFE) bonded electrode.

Porous sintered electrodes consist of a powdered metal sintered into a plaque such as the Bacon molten alkali electrolyte fuel cell (AFC) and the MCFC. In porous metal sintered electrodes the three-phase (solid, liquid and gas) interface is provided by allowing the electrode partial filling contact with electrolyte during fuel cell operation by inducing a difference between the gases and electrolyte or by limiting the amount of the electrolyte as in the MCFC. The differential pressure between the gas and the electrolyte needs to be controlled to maintain the optimum reaction interface conditions between the phases.

As for the gas diffusion or PTFE bonded electrodes that were developed for the solid polymer electrolyte (SPE also know as the proton exchange membrane or PEM) fuel cells used to power the Gemini missions orbiter AFC and PAFC. The gas diffusion electrodes consist of metal blacks or hydrophobic carbon supported metal catalysts. These are blended with fine particles of hydrophobic PTFE that flow and bind the structure as a result of heating during fabrication. During the fuel cell operation, catalyst performance and utilization is improved as some of the pores are filled with electrolyte and together with the unfilled pores provides a large vapour/ liquid interfacial area (and short diffusion paths for O_2) thereby increasing the reaction interface. The high forces existing in the small pores ensure a stable interface. The short diffusion paths are of significance where the oxygen solubility is low.

2.3.1 Models Proposed

Rocket and Brown [67, 68] treated a porous sintered metal electrode as an idealized model consisting of a single tubular pore coated with a thin film of electrolyte. On the

electrolyte side, the fine pore region is exposed to the electrolyte whereas the coarse pore region on the gas side is covered with a thin film that is thinnest at the gas entry compartment. They took into account the polarizations due to axial transport of OH^- ions and dissolved oxygen diffusion across the film, chemical reaction at the electrode-electrolyte interface and electrolyte ohmic losses. Their thin film model [67] predicted that the current density was proportional to the geometric mean of a local current characteristic (exchange current or characteristic diffusion current) and an electrolyte property (electrolyte conductivity or electrolyte species diffusion rate), only one of which was proportional to the partial pressure of oxygen (P O_2) on approaching limiting currents. The thin film model predicts $i \alpha \sqrt{P\ O_2}$. Their model predictions agreed with half cell data using diluted O_2/N_2 gases in 60-85% KOH and temperature range 150-250 ^oC as observed from the linear plot of cathode polarization verses current normalized to $\sqrt{P\ O_2}$. In the case of the flooded pore model [68] for the anode, their model predicts that $i \alpha \sqrt{i_o i_{D\ (hydrogen)}}$ (where $i_{D\ (hydrogen)}$ is the characteristic hydrogen diffusion current). Both Io and $i_{D\ (hydrogen)}$ are proportional to $P_{hydrogen}(H_2)$. Once again their theory fitted the half cell data with values of solubility-diffusivity much higher than that for hydrogen in KOH, indicating an alternative diffusion mechanism.

Srinivasan et al. [69] further expanded the model to consider activation, concentration and ohmic polarizations and recommended a circulating electrolyte system. Will [70] studied the oxidation of hydrogen on partially immersed platinum (Pt) electrodes in acid solutions that served as an ideal model for the gas diffusion electrode. In his treatment of the concept of rate limiting molecular diffusion of H_2, he estimated the relative

importance of the thin film, the length of the reaction zone and thickness of the film, the true current density and the surface diffusion of hydrogen.

Brown and Horve [71] also modified the thin film model for PTFE bonded electrolytes describing them as consisting of porous and electronically conductive platinum black agglomerates of 1-10μm diameter coated with an electrolyte film and gas filled PTFE channels 0,2μm diameter electrolyte particles.

Giner and Hunter proposed a model for PTFE bonded electrodes in which they assumed that the platinum black agglomerates (cylinders) were flooded; when current was drawn, the reactant diffused through the hydrophobic channels, dissolved in the electrolyte which were composed of agglomerates then diffused to the active sites to react. Their measurements indicated that the catalyst area in contact with the electrolyte was independent of whether it flooded and that the micro-porosity of the agglomerates was as high as 90%. They recommended the use of small agglomerates (<1 μm) and agglomerates that had only their surface catalyzed. This model was developed further and refined by Cutlip and Iczkowski [72] with the inclusion of thin film and lumped resistance effects.

These models provided the basis for development and refinement for PEMFC.

2.3.2 Ideal Electrode Requirements

Ideal or close to ideal electrode structure can be defined as one that maximizes the active surface per unit mass of the electro-catalyst and per unit electrode area, minimizes

barriers to reactant transport to the catalyst and gives invariant performance with time under actual operating conditions. Invariant performance includes voltage at constant current load, requires mechanical integrity and dimensional stability for the electrode. It is possible to conceptually describe properties that an ideal electrode should exhibit to achieve high performance but difficult to stipulate the specific properties required of each component to give this performance. The catalyst in the electrode structure should not be buried under the support. Catalyst particles must have an ionic pathway for protons that should present a low barrier to O_2 permeability, a low resistance for proton transport (high conductivity) and a low barrier to water diffusion (hydrophilic pathways for removal of product water). Catalyst particles are required to be electronically connected to the external circuit. The electrode structure should have hydrophobic gas passages to deliver and distribute reactants to the catalyst particles. The gas diffusion layer should provide mechanical support and electrical contact, optimal distribution of reactant gases and a pore structure suitable for the removal of liquid or vapour phase water.

2.3.3 Carbon Black

For fuel cell catalysts, carbon blacks are exclusively used to provide a support for the dispersion of platinum crystallites. As a catalyst support, carbon black provides electrical conductivity, thermal conductivity, low thermal expansion and a porous-permeable high surface area structural medium for transport of gases and water. It can be subjected to a wide range of voltages (0-1 V), humidified reducing and oxidizing gases as well as from freezing to moderately high temperatures (-40 to 90°C) in the PEMFC environment. The physical, chemical and electrochemical properties have to be carefully considered in the

selection of a carbon support. Carbon is thermodynamically unstable to oxidation over most of the fuel cell operating regime (>0,4V), but the kinetics are slow at the moderate temperatures and voltages found in the PEMFCs. The mechanism of electrochemical oxidation of carbon has been studied [73, 74] and involves the lattice oxidation of carbon, hydrolysis of the oxide and finally a disproportionate reaction that results in CO_2 and carbon surface oxides. Heat treatment of carbon black to 2200-2700 ^{o}C shows an ordering of the structure through a process of movement and rearrangement of carbon layer planes to form graphite structures that are found to have lower corrosion currents. Carbon blacks with a wide range of BET surface areas are commercially available viz Ketjen Black ($800m^2g^{-1}$), Vulcan ($220m^2g^{-1}$), graphitized Vulcan ($80m^2g^{-1}$), acetylene black ($70m^2g^{-1}$) and Black Pearls ($1500m^2g^{-1}$). The choice of carbon black for the PEMFC electrodes will depend on the particular requirements of the performance and lifetime expected of the stack [75, 76, 77].

2.3.4 Catalysts

Platinum supported on carbon black is the catalyst of choice at present for PEMFC cathodes. The techniques used in the preparation of supported platinum catalysts include impregnation, colloidal adsorption and ion-exchange techniques. The specific activity and exchange current density (i_o) of platinum for the oxygen reduction reaction (ORR) in pure Nafion® has not yet been defined to the same precision as in liquid electrolytes but is close to but higher than the upper limit of values reported in a liquid acid electrolyte. The i_o for the ORR of platinum-Nafion falls in the range approximately 10^{-7}-10^{-9} Acm^{-2} when corrected to ambient pressure and 65 ^{o}C [78, 79]. The exchange current density i_o exhibits Arrhenius behaviour with temperature and also depends on relative humidity in

the fuel cell. Slopes obtained from Arrhenius plots and mass specific current densities for the ORR on platinum-Vulcan have been reported to give activation enthalpies of 20-25 kJ mol^{-1} [80, 81]. Tafel slopes for platinum-Nafion have been reported in the literature in the range 60-70mV dec^{-1} [81, 82]. It has been suggested that the activity of platinum in PEM which is higher than in sulphuric and phosphoric acids partly due to reduced anion adsorption. The effect of platinum particle size on ORR such as occurs in liquid acid electrolytes with strongly adsorbing anions such as phosphate or sulphate has not been demonstrated in PEMFCs, decay in activity as a result of recrystallization of platinum crystallites analogous to that demonstrated in liquids has been observed in PEMFCs [83, 84]. The high wt% of approximately 50 for platinum-carbon (Pt/C) has allowed the fabrication of electrodes that are extremely thin (viz a 10μm catalyst layer thickness for a 0,4 mg cm^{-2} loading), which offered low ionic and mass transfer resistance and generate high power densities [84].

2.3.5 Hot-Pressing/Assembly of MEA

Electrodes or catalyst layers are commonly fabricated as independent units by the decal technique or coated directly onto the membrane or gas diffusion layer (GDL). The glass transition temperature of Nafion is approximately 150 ^{o}C (where it starts flowing) and governs the hot pressing temperature of the electrodes to the GDL or membrane. At temperatures much lower than the glass transition temperature of the membrane (approximately 140 ^{o}C) the Nafion or $CsHSO_4$ will not flow and form good ionomeric contact with the catalyst, resulting in poor utilization whereas casting of the film at higher temperatures reduces ionomer solubility but increases its robustness. Temperatures above 100 ^{o}C results in loss of water retention properties in both cesium membranes and

especially Nafion where acid catalyzed degradation of the ionomer occurs as well as partial delamination of the electrode from the membrane and the electrode is therefore preferably applied to a melt-processable form of Nafion. Thus hot pressing is generally performed at pressures of the order 5000-15000 kpa, temperatures of 120-160 ^{o}C and time periods of approximately 1-5 minutes.

CHAPTER 3

3. EXPERIMENTAL

The solid acid composite membranes were manufactured with certain properties to withstand the experimental conditions they would be subjected to during testing. The characterization thereof was necessary to observe the changes the membrane underwent when subjected to conditions similar to those of a working fuel cell at intermediate temperatures. To obtain maximum conductivity at optimum conditions, the membranes' mechanical strength was observed using analytical techniques similar to that of characterization.

3.1 CHARACTERIZATION METHODS

The following methods were used:

- Thermal Gravimetric Analysis (TGA)
- X-ray Diffraction (XRD)
- Infrared Spectroscopy (IR)
- Scanning Electron Microscopy (SEM)

3.1.1 Thermal Gravimetric Analysis

Thermal gravimetric analysis gives an indication of the solvent content of the compound at the temperature it can be released. In the case of membrane composites, the presence of different constituents each with varying properties relating to solvents embedded in the substance with each solid component possessing different melting points, complicates the release of the moisture influences the conductivity of the solid acids. Moisture in solid samples is mainly due to the equilibrium between water as the moisture content and the

atmosphere. Due to the hygroscopic nature of the sample, the relative humidity and the ambient temperature at the time of analysis need to be taken into account. The types of water in solids include essential and non-essential water. Essential water in a compound in its solid state forms an integral part of the molecular or crystalline structure. An example of essential water is water of crystallization. A second type of essential water is water of constitution usually found in compounds that yield stoichiometric amounts of water when heated or decomposed. The solid due to physical forces on the other hand, retains non-essential water. A type of non-essential water is adsorbed water, which is retained on the surface of the solid. Adsorption of water occurs in varying degrees in all solids. The amount of water adsorbed is not dependent on the humidity, temperature, and the specific area of the solid. A second type of non-essential water is called sorbed water. This type occurs in colloidal substances such as silica gel. Compared to adsorption, the quantity of sorbed water is much greater as much as 20% or more of the total weight of the solid. With sorbed water, the appearance of the solid seems dry. The sorbed water is held as a condensed phase in the solid where the quantity is largely dependent on the temperature and humidity [34].

3.1.2 X-Ray Diffraction Analysis

A greater displacement is created where peaks or troughs coincide and a smaller displacement where peaks coincide with troughs. Classical electromagnetic theory states that the intensity of electromagnetic radiation is proportional to the square of the amplitude of the waves. Thus the regions of constructive and destructive interference, is displayed as areas of enhanced and diminished intensities. Diffraction is the interference

phenomenon caused by an object in the path of the waves. A diffraction pattern results from the pattern of varying intensity caused by the interference. For the determination of structures of molecules and solids, the diffraction of waves by atoms and molecules is used effectively for this purpose. X-rays are electromagnetic radiation with wavelengths below 100 nm. Bombarding a metal with high- energy electrons produces the radiation. The electrons slow down as they plunge into the metal and generate radiation with a continuous range of wavelengths called Bremsstrahlung. Superimposed on the continuum are a few high-intensity sharp peaks. These peaks arise from an incoming electron colliding with an electron in the inner shell and eject it, and an electron of higher energy drops into the vacancy, emitting the excess energy as an X-ray photon. The earliest approach to the analysis of diffraction patterns produced by crystals was to regard a lattice plane as a mirror, and to model a crystal as stacks of reflecting lattice planes of separation d. The model makes it easy to calculate the angle the crystal must make to the incoming beam of X-rays for constructive interference to occur. It has also given rise to the name reflection, to denote an intense spot arising from constructive interference. The path length difference of two rays is given by

$AB + BC = 2d \sin \theta$ ……..Equation 3.1

where θ is the glancing angle. In numerous cases the glancing angles' path length difference is not an integral number of wavelengths, and the waves interfere destructively. But when the pathlength difference an integral number of wavelengths ($AB + BC = n\lambda$), the reflected waves are in phase and interfere constructively. This should result in a bright reflection when the glancing angle satisfies the Bragg Law

$n\lambda = 2d \sin \theta$ …….Equation 3.2

Reflections with $n = 2$ is called second order, $n = 3$, third order, and so on the nth order reflection arising from the (*nh, nk, nl*) planes. First order is assumed. In more recent applications it is quite normal to absorb the n into d and to write the Bragg Law as

$\lambda = 2d \sin \theta$ ……Equation 3.3

The primary function of Bragg's Law is the determination of the spacing between layers in the lattice, because, once the angle θ corresponding to a reflection has been determined, d may easily be established through calculation.

Laue's original powder method consisted of passing a broad-band beam of X-rays into a single crystal and recording the diffraction pattern photographically. The rationale was that a crystal would not be suitably orientated to serve as a diffraction grating for a single wavelength. Irrespective of its orientation, the Bragg law would be adhered to with respect to one of the wavelengths if several wavelengths were used. Peter Debye, Paul Scherrer and Albert Hull developed another technique. They used monochromatic radiation and a sample in a powder form. For powder samples few of the crystallites would be orientated, satisfying the Bragg law for each set of planes (hkl). For example, some of the crystallites will be positioned so that their (111) planes of spacing d_{111} result in a diffracted intensity at the glancing angle θ. The crystallites which have the glancing angle, lie at all possible angles around the incoming beam. The diffracted beams lie on a cone around the incoming beam of half angle, 2θ. The other crystallites would be positioned with different angles satisfying Bragg's law. These crystallites produce a cone of diffracted intensity with a different half angle. The underlying principle is that each set of (hkl) planes produces a diffraction cone, because some of the randomly orientated

crystallites in the sample will possess the correct angle causing diffraction of the incident beam.

Ionic Crystals. **W**here stacks of spheres model compounds containing crystals of monatomic ions, it is essential to allow for the different ionic radii (generally with the cations smaller than the anions) and different charges. The coordination number of an ion is the nearest neighbour of opposite charge. Cations and anions may have different environments in the same crystal. Even if, by chance, the ions have the same size, the problems of ensuring that the unit cells are electrically neutral make it impossible to achieve 12 close-packed structures. As a result, ionic solids are generally less dense than metals. The best packing that can be achieved is the eight-coordination of the caesium-chloride structure in which each cation is surrounded by eight anions and each anion is surrounded by eight cations. In the cesium chloride structure, an ion of one charge occupies the centre of a cubic cell with eight counter-ions at its corners. The structure is adopted by CsCl itself and by CsBr, CsI, CaS, CsCN (with some distortion), and CuZn.

3.1.3 Infrared Spectroscopy

When a beam of electromagnetic radiation of intensity I^o is passed through a molecule , it can either be absorbed or transmitted depending on its frequency and the structure of the molecule it encounters. When a molecule absorbs radiation it gains electromagnetic radiation energy as it undergoes a quantum transition from one energy state ($E_{initial}$) to another (E_{final}). The frequency of the absorbed radiation is related to the energy of the transition by Plank's law: $E_{final} - E_{initial} = E = h\nu = hc/\lambda$. Thus if a transition exists which is related to the frequency of the incident radiation by Plank's constant then the radiation

can be absorbed. If the frequency does not satisfy the Plank expression, then the radiation will be transmitted. The type of absorption spectroscopy depends upon the type of transition involved and accordingly the frequency range of the electromagnetic radiation absorbed. If absorption is accompanied by a transition from one rotational energy level to another then the radiation is from the microwave portion of the electromagnetic spectrum and the technique is microwave spectroscopy. If the transition is from one vibrational energy level to another, then the radiation is from the infrared portion of the electromagnetic spectrum and the technique is known as infrared spectroscopy. If the transition alters the configuration of the valence electrons in the molecule, then the radiation is from the ultraviolet-visible portion of the spectrum and the technique is ultraviolet-visible, or electronic absorption, spectroscopy.

Data concerning energy migration and localization in molecular layers forms the underlying understanding of many important processes involving electronic excitations or multi-vibrational excitation and bond breaking at surfaces. This is evident in the Si (111) and Si (100) surfaces. Here inelastic tunneling produces multiple vibrational excitations and Si-H bond breaking. The Si-H bond anharmonicity tends to localize the vibrational energy to a single Si-H bond by inhibiting the lateral spreading of the vibrational energy thereby increasing the opportunity for bond breaking. There are, in general, several types of motion that a molecule may undergo.

First, the molecule as a whole may move through space in some arbitrary direction and with a particular velocity. This type of motion is called translational motion and with it we associate the translational kinetic energy of the molecule, given by $mv^2/2$ (v = velocity of the center of mass of the molecule). The velocity with which a molecule

translates may be resolved into components along each of the three axes of a Cartesian coordinate system, so that we may write $mv^2/2 = mv_x^2/2 + mv_y^2/2 + mv_z^2/2$, where v_x is the x-component of velocity, etc., and m is the mass of the molecule. This equation tells us that we may consider the total translational KE of the molecule to be made up of three parts, each of which represents the kinetic energy of the molecule along one of the reference directions. Since any translation of the molecule may be considered to arise from the vector sum of its motions along the three axes, the kinetic energy may always be broken up into the sum of three contributions, one arising from motion along the x axis, one from motion along the y axis, and one from motion along the z axis. We characterize this situation by saying that the molecule has 3 translational degrees of freedom, one corresponding to each Cartesian axis.

Second, the molecule may rotate about some internal axis. Again, any such axis may be resolved into components along the x, y, and z-axes of a Cartesian coordinate system so that any rotation of the molecule may be resolved into three mutually perpendicular components. The rotational kinetic energy of the molecule can then be written

$KE_{rot} = I_x\omega_x^2/2 + I_y\omega_y^2/2 + I_z\omega_z^2/2$ ……Equation 3.4

where Ix, Iy, and Iz are the moments of inertia about the x, y, and z axes, and ω_x, ω_y, and ω_z are the angular velocities about these axes. Again, then, we see that there are in general 3 degrees of freedom associated with rotational motion, one corresponding to each Cartesian axis. An exception to this generalization arises in the case of a linear molecule for which one of the three axes is normally taken as the molecular axis. Consider, for example, the diatomic molecule shown in the figure below. The molecule is

shown with its bond axis coincident with the z axis of a coordinate system. In this case, the molecule

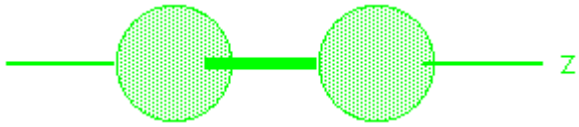

Figure 3.1: A diatomic molecule with its bond axis coincident with the z axis.

has no rotational energy about the z axis, because the moment of inertia about this axis is zero. For linear molecules then, there exist only two rotational degrees of freedom, rather than 3.

Finally, the molecule may vibrate. A diatomic molecule, for example, vibrates by repeated stretching and contraction of the bond joining the two atoms, as shown below:

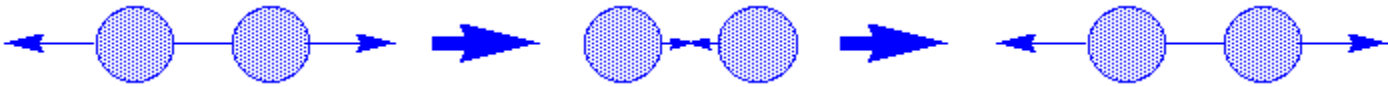

Figure 3.2: A diatomic molecule depicting the bond vibrations.

Such a molecule has, in addition to 3 translational and 2 rotational degrees of freedom, one vibrational degree of freedom. In general, for a polyatomic molecule, we may deduce the number of vibrational degrees of freedom (sometimes called vibrational modes) by subtracting the number of translational and rotational degrees of freedom from the total number of degrees of freedom possessed by the molecule. The latter number is simply 3N, where N = the number of atoms in the molecule. (Realize that each atom may independently move in any of the three directions. Each atom has, therefore, 3 degrees of freedom available to it, with a total of 3N for the molecule.) This leads us to the general

rule that the number of vibrational degrees of freedom is given by 3N-6 for a non-linear polyatomic molecule; and by 3N-5 for a linear polyatomic molecule. According to this rule, the water molecule which is a non-linear molecule with N = 3, should have 3 vibrational degrees of freedom-in other words, it should undergo three independent types of vibration. These are shown below.

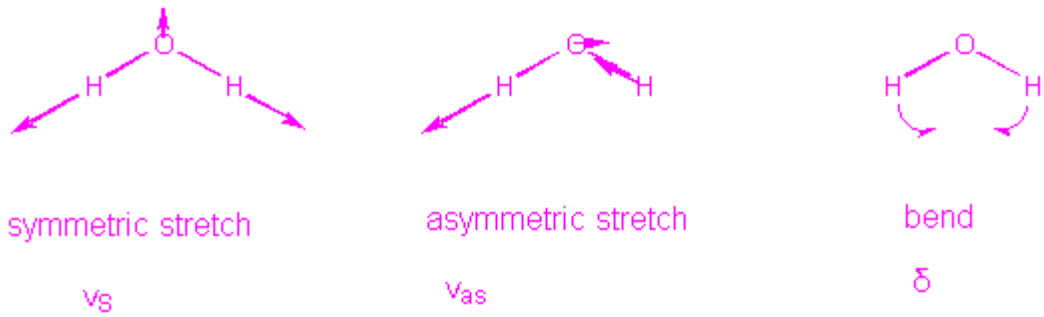

Figure 3.3: A water molecule depicting three types of vibration.

The arrows show the directions in which the atoms move during the vibration.

Each of the vibrational motions of a molecule occurs at a certain frequency, which is characteristic of the molecule and of the particular vibration. The energy involved in a particular vibration is characterized by the amplitude of the vibration, so that the higher the vibrational energy, the larger the amplitude of the motion. According to the results of quantum mechanics, only certain vibrational energies occur to the molecule (the same may be said of rotational and translational energies), and thus only certain amplitudes occur. Associated with each of the vibrational motions of the molecule, there is a series of energy levels (or vibrational energy states). The molecule may be made to go from one energy level to a higher one by absorption of a quantum of electromagnetic radiation, such that $E_{final}-E_{initial} = h\nu$. In undergoing such a transition, the molecule gains vibrational

energy, and this is manifested in an increase in the amplitude of the vibration. In the case of visible radiation the frequency of light required to cause a transition for a particular vibration is equal to the frequency of that vibration, so that we may measure the vibrational frequencies by measuring the frequencies of light which are absorbed by the molecule. Since most vibrational motions in molecules occur at frequencies of about $10^{14}sec^{-1}$, then light of wavelength = $c/\lambda = 3 \times 10^{10}$ cm/sec/$10^{14}sec^{-1} = 3 \times 10^{-4}$ cm = 3 microns will be required to cause transitions. As it happens, light of this wavelength lies in the so-called infrared region of the spectrum. IR spectroscopy, then, deals with transitions between vibrational energy levels in molecules, and is therefore also called vibrational spectroscopy. An IR spectrum is generally displayed as a plot of the energy of the infrared radiation (expressed either in microns or wave numbers) versus the percent of light transmitted by the compound. This is indicated schematically below.

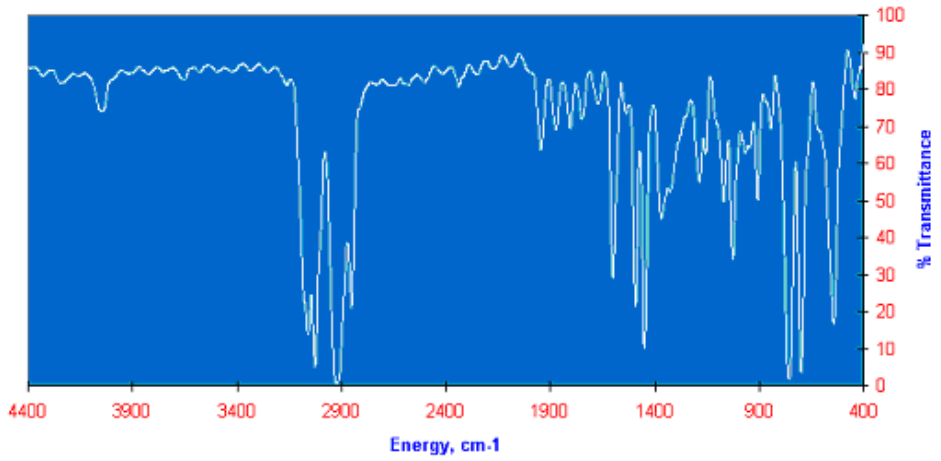

Figure 3.4: A typical IR spectrum.

Within this energy range the spectrum of the molecule will appear as a series of broad absorption bands of variable intensity, each of which brings to the viewer some piece of structural information. Each absorption band in the spectrum corresponds to a vibrational transition within the molecule and gives a measure of the frequency at which the vibration occurs. For the water molecule, for which there are three vibrational degrees of freedom, there are consequently three sets of energy levels within which transitions may occur. These are shown below, along with the particular vibration corresponding to each.

Figure 3.5: A water molecule depicting 3 sets of energy levels and possible vibrations.

Note that the spacing between energy levels depends upon the particular vibration being considered. Each spacing requires a photon of different energy to cause the transition, so we expect photons of three different energies to be absorbed by H_2O. This is found to be the case the frequencies of the photons (hence of the vibrations) occurring at 3500 cm^{-1}, 1650 cm^{-1}, and 600-300cm^{-1}, respectively.

The fact that a molecule vibrates does not in itself insure that the molecule will exhibit an IR spectrum. In order for a particular vibrational mode to directly absorb infrared

electromagnetic radiation, the vibrational motion associated with that mode must produce a change in the dipole moment of the molecule. Hydrochloric acid HCl, for example, with a center of positive charge located near the H atom indicated as H^+ and a center of negative charge located near the Cl atom indicated as Cl^-, has a dipole moment. Moreover, the magnitude of the dipole moment will change, as the HCl bond stretches, and this vibration will absorb IR radiation. HCl will exhibit an IR spectrum and is thus termed an infrared active molecule. The N_2 molecule, on the other hand, has no dipole moment. Furthermore, stretching the N-N bond will not produce a change in dipole moment, so this molecule is infrared inactive (i.e. cannot directly absorb IR radiation). It is important to realize that there are many molecules which, although possessing no permanent dipole moment, still undergo vibrations which cause changes in the value of the dipole moment from 0 to some non-zero value. Consider the CO_2 molecule:

Figure 3.6 A CO_2 molecule and corresponding dipoles.

This molecule obviously has no permanent dipole moment, since the individual bond dipoles exactly cancel each other. However, when the molecule undergoes a bending vibration, as shown below, its dipole moment changes from zero to some non-zero value:

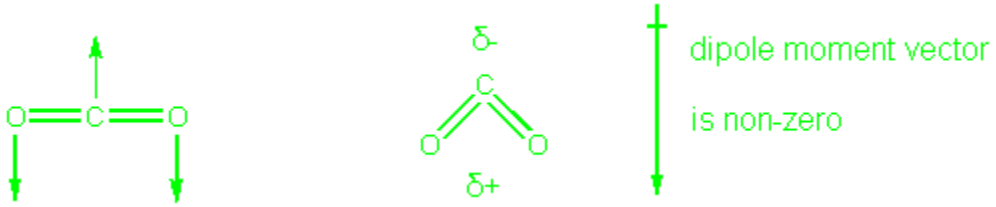

Figure 3.7 A CO_2 molecule and changes in the dipole moment.

This vibration produces a change in dipole moment and the molecule is therefore IR active. For the vibrations of the water molecule illustrated earlier, a little study will show

that all three types of motion lead to a change in dipole moment. Hence all three vibrations of the water molecule are IR active and we expect that each will give rise to an absorption band in the IR region. We have already seen that this expectation is borne out.

The requirement that a vibration must cause a change in the dipole moment of the molecule in order to absorb radiation can be understood if we realize that exchange of energy between electromagnetic radiation and matter can occur only if the radiation and matter can interact (or couple) in some way. Electromagnetic radiation consists of perpendicular electric and magnetic fields, which oscillate sinuosoidally at the frequency of the radiation.

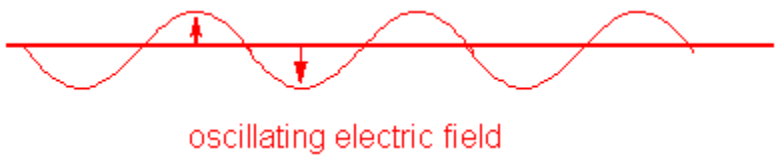

Figure 3.8 The electric oscillation is shown as a sine wave.

Note that this oscillation of the electric field is equivalent to an oscillating dipole moment. Now a molecule may interact with the radiation by interacting with the oscillating electric field, but such interaction is possible only if the molecule also possesses an oscillating electric field. Furthermore, the frequencies of the oscillations must be the same. We therefore see that if a vibrational motion of a molecule is to absorb IR radiation, the motion must generate an oscillating electric field. This is equivalent to saying that the vibration must produce a change in dipole moment. The dipole moment will oscillate at the frequency of the vibration, so that radiation of this frequency may then be absorbed.

In addition to the number of distinct vibrations to be expected for a given molecule, we can make certain general statements about where in the spectrum absorptions due to

certain types of vibrations may be expected to occur. It can be shown that for a diatomic molecule, A-B, the wave number (i.e., the reciprocal of the wavelength) of the infrared radiation absorbed by the vibration of the molecule is given by

$\nu bar = 1/2\pi\ (k_{AB}/\mu_{AB})^{1/2}$ where $\mu_{AB} = M_A M_B/(M_A + M_B)$ ……..Equation 3.5

Here k_{AB} is the force constant for the bond between A and B, and is a measure of the bond strength; and M_A and M_B are the masses of the atoms which are bonded together. We conclude from this equation that the heavier the atoms involved in the bond, the lower the absorption frequency should be, given fairly constant bond strength. We have to be careful in applying this equation, however. For the series HF, HCl, HBr, and HI, the IR absorptions occur at, respectively, 3958, 2885, 2559, and 2230 cm^{-1}. It is tempting to jump to the quick conclusion that this is a result of the increase in mass of the halogen atom. Calculation of Ea (activation energy) for each molecule, however, reveals that the reduced mass actually changes very little. The change in frequency is actually due to the decrease in bond strength along the series.

3.1.4 Scanning Electron Microscopy

The technique required the implementation of an electron microscope to study the surface and cross section of the composite membranes. A high magnification up to 3000X revealed significant data about the membrane surface that needed to be taken into account when preparing electrodes (refer to chapters 3,4 and 5).

The matrix surface and the surface and cross-section of the composite membranes morphology were investigated by means of SEM. SEM images were obtained on a Hitachi x650. The cross-sections of the composite membrane were obtained by breaking the membrane into small pieces under liquid nitrogen.

Hitachi	x650
Accelerating voltage	25kV
Aperture	0.4 mm
Tilt angle	0°
Resolution	6 nm
Working distance	15 mm

3.2 CONDUCTIVITY ANALYSIS OF THE SOLID ACID COMPOSITE MEMBRANE BY IMPEDANCE

3.2.1 Frequency Response Analysis

The frequency response analysis was performed to measure the impedance of the membrane and thus determine the conductivity, where $\sigma=1/\Omega$, at different temperatures. Placing the membrane inside a fuel cell, which is manufactured using hardened stainless steel, performed the thermally regulated conductivity analysis, and can withstand temperatures above 300°C (573K). Heating cartridges were placed inside the fuel cell housing and were connected to a temperature controller. A probe connected to the temperature controller was placed inside the fuel cell housing to allow for temperature feedback to the temperature controller. The fuel cell is divided into two halves-each made electrically independed of the other made possible by a flat piece of Teflon cut to size to fit the surface of the fuel cell between the two metal components. The centre of

the Teflon has a 2.5x2.5cm area exposed to allow electrical contact between the electrode and the surface of the metal housing of the fuel cell.

Each half (housing) has a gold plated connector attached to it allowing the transfer of electrical stimulus frequency from the auto lab. The auto lab (PG stat30) in turn is connected to the computer data processor by means of an interface.

The flow field is the only exposed area allowing for electrical contact between the electrode and the metal surface of the fuel cell.

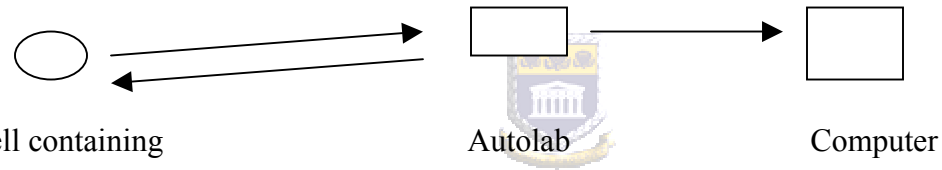

Figure 3.9 FRA was performed using the Autolab and data processor (computer)

The frequency response refers to the response characteristics of the system when that system is subjected to sinusoidal inputs. The input frequency is regulated while the output characteristics are computed or represented as a function of the frequency. FRA can thus study the MEA in the fuel cell for insights into stability and performance characteristics.

The frequency response is represented in a number of ways. The Bode plot is one where the amplitude ratio (AR) is compared to the phase lag as a function of the frequency of the input of the line wave (which is similar to the frequency of the output wave). Logarithmic scales are used for the frequency axis and the y-axis is often plotted using

the units of decibels, which is 20 log (AR). In a Bode plot, for a first order process, both the AR and ϕ (impedance) decrease as the frequency increases. At low frequencies the output is able to respond to slow varying input disturbances-in this analysis varying from 230000Hz to1.0Hz, having a small attenuation (AR close to 1). At higher frequencies though, the AR decreases rapidly-approaching an asymptote with a slope of –1 in a log-log graph, for first order self-regulating processes. Impedance spectroscopy is often used for the study of electrochemical systems [34-40]. The advantage of this technique is the immittance plots of the dispersion that offer good visual data about the characteristics of the electrochemical system. The dispersion is normally analysed by means of an equivalent circuit as model, where the various circuit elements are related to the respective processes in the system (e.g. ionic conductivity, double layer capacitance and Warburg diffusion among others). In most cases the circuit parameters are extracted using simple graphical means. The drawback relates to the time constraints of the respective sub-circuits, which are relatively close together and the frequency dispersion cannot be divided into distinct separate regions. This applies if elements with fractional power dependence on frequency are present such as Warburg or Constant Phase Elements (CPE) [41-43]. The modulus of such an element, which is sub-linear with frequency, extends its influence over a large frequency range in the dispersion. For these instances, all circuit parameters should be adjusted simultaneously to fit the equivalent circuit response to the measured dispersion. This is made possible by the use of the special Non-linear Least Squares Fit (NLLSF) procedure [44-45]. For the use of such a NLLSF procedure one has to know the shape of the equivalent circuit and have a set of adequate starting values for the adjustable circuit parameters. An immittance diagram should be

able to supply this information. The most prominent parts are located first and the corresponding elements are removed from the circuit by subtracting their dispersion from the overall frequency dispersion.

Crude values for the adjustable parameters are obtained through simple graphical means. The interface response of an ionic conductor can often be modelled as a total ionic resistance (grain boundary + ionic resistance) in series with a constant phase element at times combined with a capacitor [46]. In this partial dispersion of the impedance representation, a suitable point is selected through which a tangential line is drawn. The intersection with the real axis gives the total resistance while the fractional exponent, n, of the CPE is found from the slope. The dispersion relation for the CPE is given by [43],

$Y^*(\omega) = Y_o \cdot (j\omega)^n$

The factorY_o is found from the imaginary value of the selected data point, Z_i":

$Y_o = [-\sin n/\pi] / Z_i" \times \omega^n_i$

An approximate value for the capacitance can be found by subtracting the low frequency limit, ω_I, the calculated CPE response from the imaginary part of the measurement, Z_i":

$C = 1/\omega_I [Z_i" - \omega_I^{-n} \times (\sin n\pi/2)/Y_o]$

A procedure similar to this one is used for the analysis of the bulk response at the high frequency limit of the dispersion, but now in the admittance representation. This is important to note that a resistance in parallel with a CPE and/or capacitance is obtained. When there is little interference with the dispersion of the adjacent sub-circuit, these values can be used for a subsequent simple NLLS-fit by the program. Another option could be that the parameters for the adjacent sub-circuit must be obtained in order to perform a NLLS-fit for the combined sub-circuits. For this reason, the CPE (and

capacitance) dispersion is removed from the total dispersion, thus exposing the dispersion of the adjacent sub-circuit.

3.3 PREPARATION METHODS

3.3.1 The cesium hydrogen sulphate ($CsHSO_4$) was prepared as follows:

Cs_2CO3 as precursor:

3.3.1.1 Method 1:

25.0g $CsCO_3$ (99,9%) was dissolved in 200 ml water in a reaction vessel. 15 ml 98% H_2SO_4 in 200 ml water was added to this solution, drop wise, by means of a burette. Total volume was 400 ml. The solution was stirred for 24 hours overnight. The solution was then heated in an oven at 105°C until it formed a thin flaky top layer and hard solid amorphous bottom layer. The solid mass adhered to the reaction vessel.

3.3.1.2 Method 2:

25.0g $CsCO_3$ (99,9%) was dissolved in 200 ml water in a reaction vessel. 15 ml 98% H_2SO_4 in 200 ml water was added to this solution, drop wise, by means of a burette. Total volume was 400 ml. The solution was stirred for 24 hours overnight. Omitting the

drying procedure of Method 1 and adding a suction procedure to dry the crystals as the previously heated crystals resulted in incomplete drying that was time consuming and the crystals formed were then returned to the soluble form and adhering to the reaction vessel. Once the crystals were dried by suction for 30 minutes, further drying for 3 hours at 105°C under vacuum (-100 kpa) ensured the complete removal of water from the surface of the crystals.

3.3.2 Preparation Method Using Cesium Sulphate(Cs_2SO_4) as precursor

$CsHSO_4$ was also prepared using Cs_2SO_4 as a precursor. The motivation was to compare the performance of the solid acid with respect to conductivity and mechanical properties, with that of the Cs_2CO_3 as precursor to $CsHSO_4$.

3.3.2.1 Method 1:

Dissolved 35.3g Cs_2SO_4 (Grade1, 99%) in 200 ml water. Diluted 21.7g H_2SO_4 (98%) in 50 ml water. Slowly added the dilute sulphuric acid solution drop-wise to the cesium sulphate solution prepared above while stirring at 250 rms and heating the solution to 60°C. The crystals formed were $CsHSO_4$.

3.3.3 The cesium dihydrogen phosphate was prepared as follows:

The cesium dihydrogen phosphate was prepared by varying the concentration of precursor additives used to strengthen the membrane and add support to the electrolyte. The reaction time and temperatures were also adjusted to ensure optimum product yield and formation of CsH_2PO_4 with respect to structure.

3.3.3.1 Method 1:

Dissolved 25.0g $CsCO_3$ (Grade1, 99%) in 200 ml water. 15 ml 98% H_3PO_4 previously dissolved in 200 ml water was added to the solution prepared above, drop wise, by means

of a burette. Total volume was 400 ml. The solution was stirred for 24 hours overnight. The solution was then heated in an oven at 105°C until it formed was a thin flaky top layer and hard solid amorphous bottom layer.

3.3.3.2 Method 2: Change in total volume

Dissolved 25.0g $CsCO_3$ in 200 ml water and added 15 ml 98% H_3PO_4. The solution was then stirred for 24 hours. Total volume was 200 ml. The resulting solution was then heated in an oven at 105°C until a wet crystalline precipitate was formed. The precipitate was a wet shiny continuous mass.

3.3.3.3 Method 3: Addition of PTFE and Silica

To 7,0014g of wet crystal precipitate produced in method 2 was added 2.0091g PTFE powder and 0.5012g fumed silica 380, and all ground together. With the addition of water, a final volume of 400 ml was reached. It was heated to 300°C while continuously stirring, for half an hour, and then maintained at 110°C thereafter without stirring until all the solvent had evaporated.

3.3.3.4 Method 4:

Omitting the drying procedure of Method 2 and adding a suction procedure to dry the crystals as the heating resulted in incomplete drying that was time consuming and the crystals formed were then returned to the soluble form and adhering to the reaction vessel. Once the crystals were dried by suction for 30 minutes, further drying at 105°C under vacuum for 3hours ensured the removal of water from the surface of the crystals.

3.4 Membrane Electrode Assembly (MEA) and Catalytic Ink preparation

Three types of membrane electrode assemblies (MEAs) were prepared using a different membrane on each occasion i.e. (1) MEA with pure cesium hydrogen sulphate as the membrane; (2) MEA with cesium hydrogen sulphate as the proton conducting material in combination with silica and Teflon; (3) MEA with cesium dihydrogen phosphate as the proton conducting material in combination with Teflon.

3.4.1 MEA Catalytic Ink Preparation with $CsHSO_4$ as the Membrane

Using carbon cloth as the gas diffusion-backing layer (20 % water resistant PO# A111766) the CBES composition for CBES preparation B where 0.2453g 20% $CsHSO_4$ solution was added to 0.5101g Pt nominally 40% on carbon black B/No. 42204 Lot. No. A28N06 and 5.0471g H_2O (Deionized). The 20 wt% $CsHSO_4$ was prepared by dissolving 20.0g $CsHSO_4$ in 100ml deionized water. The $CsHSO_4$ was prepared with Cs_2CO_3 and sulphuric acid as the precursors. The temperature at which the compaction was performed was in the region of 140°C. The pressure that gave the more effective smooth surfaces was approximately 10bar.

CBES preparation to determine the effect of varying catalyst loading warranted the use of lower nominal 20% platinum on carbon black. The CBES preparation used included 20 wt% platinum on carbon, Pt nominally 20% on carbon black B/No. 26204 Lot. No. A22N06 and 40 wt% $CsHSO_4$Cloth type: “A” 0.35mm thick; 20% wet proof PO# A111766. The membrane was prepared by adding a 50% $CsHSO_4$ solution on to glass fibre filter paper that was then dried and crystallized at 105°C. The catalyst composition was used at the cathode and anode terminal ends. The loadings were dried at 105 ^{o}C for 2,5 hours. The appearance of cracks after the first hour was smoothed over by wetting with deionized water. The temperature was then decreased to 60 ^{o}C and the drying time

extended to 4 hours. The electrode once completely dry and crack free was subjected to an approximate temperature of 142°C for 5 minutes as a precautionary measure to ensure that the electrode surface does not crack once inside the fuel cell housing. The pre-check indicated a positive result with no cracking on the electrode surface. The proton conducting substance is pressed in a 46mm diameter stainless steel die at 400 atm at room temperature. Along with the membrane, the electrode support i.e. carbon cloth covered by a stainless steel mesh was pressed on either side of the membrane at 400atm. The carbon cloth also serves as an electron conducting material. The stainless steel mesh serves as a current collector with mesh resistance of 0,7 Ω. The stainless steel mesh was the exactly shaped to overlap the flow field in the fuel cell.

The high temperature with high catalyst loading versus high ion conductor and binder concentration was also investigated. The MEA preparation was performed at temperatures of approximately 140°C and pressures of approximately 10bar.

For the electrode assembly itself, the catalyst to binder ratio included 0,2063g 40% Pt/C and 0.6312g cesium hydrogen sulphate as binder and ionic conducting material which formed the catalytic ink which was applied to the gas diffusing backing layer. The second catalytic ink preparation included 0.1262g 40% Pt/C and 0.0545g $CsHSO_4$ as the binder and ionic conducting material. This was applied to the gas diffusing backing layer cloth type "A" 0.35mm thick which was 20% wet proof PO# A111766.

The CsH_2PO_4 used as the proton conducting membrane in the membrane electrode assembly was synthesised as in method 4 mentioned above. The $CsHSO_4$ used as the proton conducting membrane in the membrane electrode assembly was synthesised as in method 2 mentioned above.

3.4.2 MEA with $CsHSO_4$ Composite Membrane ($CsHSO_4$–SiO_2-PTFE)

Composite membranes for proton conduction: Determination of high temperature phase transition or "onset of partial polymerization at reaction sites on the surface of solids"

The tri-component membranes consist of $CsHSO_4$, PTFE and SiO_2. The composite is compacted in a 46mm diameter stainless steel die at 400 atm at room temperature. Along with the proton conductor, the gas diffusion electrode support layer i.e. carbon cloth covered by a stainless steel mesh is pressed on either side of the membrane. The resistance of the mesh is 0,7 Ω.

Table 3.1: Composite membrane ratio's containing $CsHSO_4$, PTFE and Electrolyte

Membrane	% Electrolyte	%Insulator	% Electrolyte Support
A	80% $CsHSO_4$	17% PTFE	3% SiO_2
B	60% $CsHSO_4$	34% PTFE	6% SiO_2
C	53%$CsHSO_4$	40%PTFE	7%SiO_2
D	57,5%$CsHSO_4$	36,5%PTFE	6%SiO_2

The membranes were extremely durable during testing. With the addition of PTFE, cyclic heating and cooling resulted in a membrane with a dry smooth surface type appearance. When heat in the region of 100 ^{o}C is applied to the composite during compaction, the powder in the compacting cell is forced out through the sides of the

stainless steel apparatus. Using a lower temperature during the compaction process prevented the powder from leaving the compaction cell.

3.4.2.1 MEA with $CsHSO_4$ and PTFE

Table 3.2: Composite membrane ratio's containing $CsHSO_4$ and PTFE

Membrane	% Electrolyte	%Insulator
E	60%$CsHSO_4$	40%PTFE
F	70%$CsHSO_4$	30%PTFE
G	50%$CsHSO_4$	50%PTFE
H	90%$CsHSO_4$	10%PTFE

Similarly to the composites prepared above, these composites were pressed in a 46mm diameter stainless steel die at 400 atm at room temperature. Along with the $CsHSO_4$ powder, the electrode support i.e. carbon cloth covered by a stainless steel mesh, was pressed on either side of the membrane at 400 atm as well. The resistance of the mesh was 0,7 Ω. The process was similar to that of component composite formation. The PTFE was pre-treated by heating at 105 ^{o}C for 3hours to remove water.

3.4.3 MEA Containing a CsH_2PO_4 Composite Membrane (CsH_2PO_4–PTFE)

In an attempt to reduce the uptake of water by CsH_2PO_4, PTFE was introduced in a composite formation. The solid electrolyte once synthesised was extremely hygroscopic. The formation of droplets on the electrolyte surface took place within 4 hours of synthesis.

CHAPTER 4

4. PURE CESIUM HYDROGEN SULPHATE ($CSHSO_4$) SALT

A characterization and conductivity comparative study of two methods of preparation of cesium hydrogen sulphate an inorganic high temperature proton conductor.

4.1 PREPARATION METHODS OF CESIUM HYDROGEN SULPHATE

Two preparation methods were employed for the preparation of $CsHSO_4$ one with Cs_2SO_4 and the other using $CsCO_3$. The $CsHSO_4$ produced by using the $CsCO_3$ as precursor (method 1) as employed in the composite formation will be reviewed in chapter 5.

4.1.1 Method 1: This method as discussed in chapter 3 (Experimental), uses Cs_2CO_3 and H_2SO_4 as precursors, producing $CsHSO_4$, CO_2 and water viz.

$Cs_2CO_3 + 2H_2SO_4 \rightarrow 2CsHSO_4 + CO_2 + H_2O$

4.1.2 Method 2: This method as discussed in chapter 3 (Experimental), uses $CsSO_4$ and H_2SO_4 as raw material, producing $CsHSO_4$ viz.

$Cs_2SO_4 + H_2SO_4 \rightarrow 2CsHSO_4$

4.2 CHARACTERIZATION BY SEM:

The $CsHSO_4$ crystals produced by these methods were analyzed by scanning electron microscopy. The morphology of the crystals using cesium sulphate as precursor appear smoother and closely packed as opposed to the more granular rough surface produced by the cesium carbonate precursor.

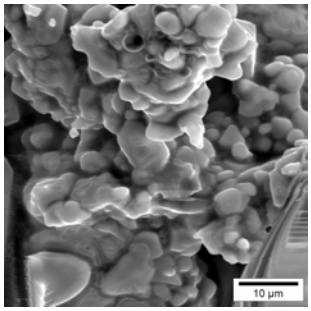

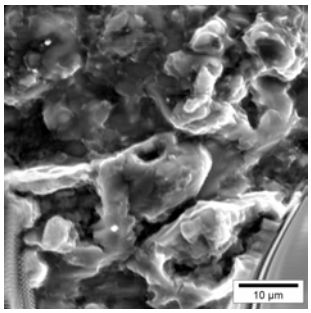

(a) Cs_2 CO_3 as the precursor (b) Cs_2SO_4 as the precursor

Figure 4.1 (a-b): SEM images of $CsHSO_4$ crystals synthesized by using Cs_2CO_3 and Cs_2SO_4 as the precursor

4.3 CHARACTERIZATION OF $CsHSO_4$ BY IR

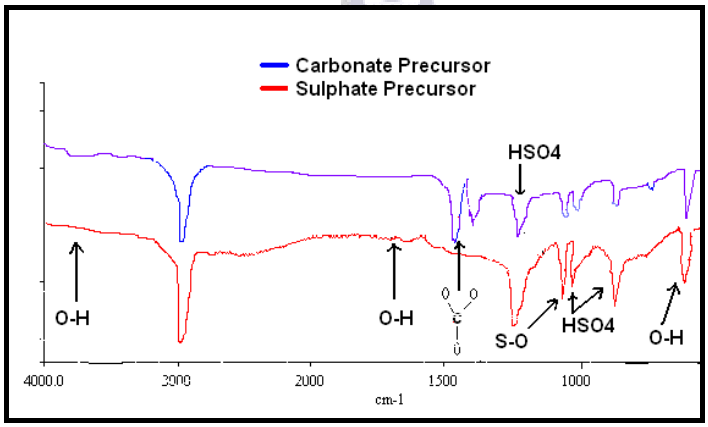

Figure 4.2: IR spectral analysis comparing the two methods of crystal preparation.

The synthesis method using Cs_2SO_4 as precursor for $CsHSO_4$ has a more defined peak spectrum in the 1000cm^{-1} region. A broad peak in the 1250 cm^{-1} region suggests the presence of the sulphate bonding. Strong transmitting bands present in the 1400 – 1500cm^{-1} region for the Cs_2CO_3 as precursor synthesis, indicate a bond. There should be more residual peaks present in the CO_3^{2-} method. The sulphate band region include, peaks of similar resolution and strength to those analyzed at room temperature. Hydroxyl bands typical in the area 3700 – 3100cm^{-1} are absent. This

indicates possible water or solvent residue loss on drying at low temperature. Slight peaks at the 1410 – 1450cm^{-1} suggests the incomplete conversion of Cs_2CO_3 in the presence of H_2SO_4 to $CsHSO_4$, as this band area is indicative of carbonates (CO_3^{2-}). With the possibility of three absorbing bands for water, each spacing requires a photon of different energy to cause the transition, so we expect photons of three different energies to be absorbed by H_2O. This is found to be the case the frequencies of the photons (hence of the vibrations) falling at 3500 cm^{-1}, 1650 cm^{-1}, and 600-300cm^{-1}, respectively.

Regardless of the type of fuel:

$H_2 + CO_3^{2-} \rightarrow H_2O + CO_2$

When a hydrocarbon fuel is used:

$CO + CO_3^{2-} \rightarrow 2CO_2 + 2e^-$

The HSO_4^- ion absorption regions are 1180-1160 cm^{-1}, 1080-1000 cm^{-1} and 880-840 cm^{-1}. Along with these bands, SO_4^{2-} absorbs in the region of 680-610 cm^{-1} and 1130-1080 cm^{-1}, which is prominent in the cesium hydrogen sulphate spectra synthesized from cesium sulphate.

4.4 CATALYST DEPOSITION ON TO THE GAS DIFFUSION LAYER FOR ELECTRODE FORMATION

4.4.1 Deposition by bristle layering: The catalyst (40 % Pt/C) in paste form with $CsHSO_4$ in water was applied to the gas diffusion layer. Technimat-Carbon Grade 6100-100; 7.6 % organic content, and contact resistance approximately 2.50 Ohms.

4.4.2 Deposition by aero-spray coating: The catalyst (40 % Pt/C) dispersed in water with a 20 wt% $CsHSO_4$ solution was applied to the gas diffusion layer. The solution was placed in a sample holder attached to an air gun. By means of high-pressure nitrogen passing through the spray apparatus, the sample is forcefully pushed through the spray nozzle and deposited onto the gas diffusion layer Technimat-Carbon Grade 6100-100; 7.6 % organic content, and contact resistance approximately 2.50 Ohms.

4.4.3 The preferred method of catalytic deposition was by bristle layering. This was an effective method as more catalyst in the paste form could be deposited onto the backing layer more efficiently and with less wastage resulting in higher loading electrodes. Whereas, in the aero-spray coating method, most of the catalyst and proton conductor-binder was lost due to inaccurate spray placement passing the backing layer and also due to dripping.

4.5 VARYING THE CATALYST AND BINDER CONCENTRATION IN THE CBES PREPARATION

For the membrane electrode assembly pure $CsHSO_4$ was used as the binder/proton conductor and solid acid proton conducting membrane along with 40% platinum on carbon as the catalyst. Varying concentrations of catalyst and binder were employed in the CBES preparations. The binder used, which possesses a very high electrical resistance towards electron conductivity, acted as an insulator in the catalytic ink compositions. The ability of the electrode to conduct the available electrons is seriously hampered by the shortage or absence of continuous conducting pathways from the oxidation reaction site to the current collector. The low resistance catalyst-

carbon deposition of Pt/C, needs to be in excess of the insulator for percolation conducting paths to form.

Table 4.1: Catalyst and binder concentrations varied by weight in ink preparations

Ink preparation	**Catalyst (Wt %)**	**Binder (Wt %)**
A	20	40
B	30	40
C	35	40
D	38	40
E	40	40
F	30	30
G	38	30
H	40	30

The catalyst concentration gives a clear indication of the catalyst loading significance to the potential (refer to fig.4.3). The potential dropped within a few minutes and a subsequent impedance check showed that the electrode had pierced the membrane. This was due to the carbon fibres protruding from the gas diffusion layer resulting in the anode and cathode touching across the membrane. The $CsHSO_4$ served a dual purpose as binder and proton conductor and varying concentrations thereof ($CsHSO_4$) showed little effect on the current and potential.

4.5.1 <u>The Membrane Electrode Assembly (MEA): For High Temperature Fuel Cells Performance of the MEA with Varying Catalyst Binder Ratios</u>

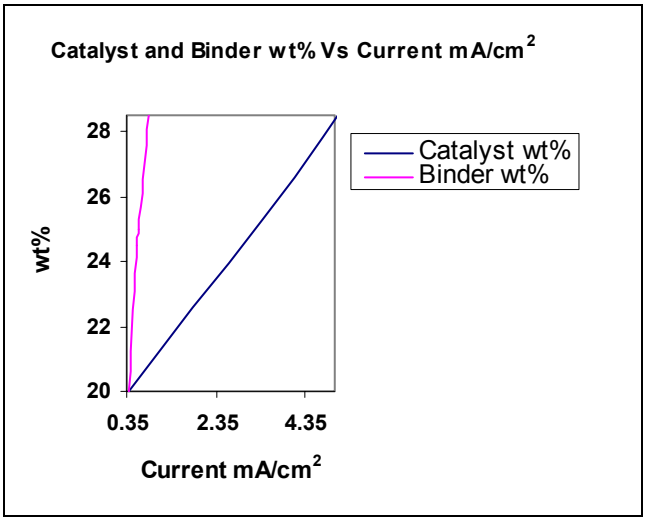

Figure 4.3: Catalyst and binder wt% relative to the current mA/cm^2.

The catalyst to binder ratio is favoured in the direction of the catalyst as no significant change in current is noted as the binder is increased. The binder is an inorganic non-conducting electron insulating material. This would oppose the percolation of the electrode conducting material. To prevent the impact this insulating material would have on a conducting electrode, the concentration of the insulating material should not affect the percolation threshold, which in the figure above is clearly not affecting the effectiveness of the catalyst.

The preparation procedure of the membrane electrode assembly was performed using a manually operated hydraulic press. The method employed to synthesize the $CsHSO_4$ which functions as the super ionic phase at temperatures above 132°C (405K), incorporates Cs_2CO_3 as the precursor. The membrane electrode assembly was composed of a CBES preparation including 40 % Pt/C. The platinum catalyst used was commercial grade (E – Tek lot. No. A28N06) consisting of 40 % platinum on carbon black and 40 wt% $CsHSO_4$ as the binder. The high operating temperatures, up to 170°C (443K), warranted the application of the dual-purpose binder and ion conductor in the form of a 20 wt% $CsHSO_4$ solution. The fuel supplied to the fuel

cell unit was methanol and hydrogen gas separately for the oxidation and subsequent proton release. Oxygen was supplied to the cathode promoting the reduction process producing water as the environmentally-friendly end product. A drop in ionic resistance at around 142°C was indicative of the super-ionic phase transition. The resulting current was 0.4mA.

After heating the $CsHSO_4$ membrane in the presence of hydrogen gas as:

$2CsHSO_4 + 4H_2 \rightarrow Cs_2SO_4 + H_2S + 4H_2O$ ……..1

(Platinum catalyst)

There were signs of $CsHSO_4$ degradation at around 140°C (413K) upwards. The presence of an unpleasant smell-that of H_2S-supported reaction 1. Based upon the decomposition reaction, one would anticipate a weight loss 21.3% for $CsHSO_4$ in the presence of platinum/carbon catalyst.

In the absence of H_2(g):

$2CsHSO_4(s) \rightarrow Cs_2SO_4(s) + SO_3 + H_2O(g)$…….2

(Platinum catalyst)

The reaction is mainly due to adsorbed water and volatile impurities. This is of significance when methanol is introduced. Reaction 2 is unlikely when H_2 is absent [65].

From the experimental evidence of an unpleasant smell reaction 1 seems more likely to have occurred. Also the platinum catalyst catalyses the decomposition reaction of $CsHSO_4$ and lowers the decomposition temperature.

With the increased catalyst concentration (40 % Pt/C) kept constant, so as to note the effect of the ion conductor by varying the concentration of the cesium hydrogen sulphate, on the overall potential and current was expected to be either enhanced or lowered. The procedure was reversed and the difference was minimal with catalyst

loading half of the normal loading. The current was 6 mA for the lower catalyst loading and 9 mA for the higher catalyst loading. The potential was 110mV in each case.

The proton exchange membrane was reinforced using insoluble but insulating non-conducting type material (see below, Chapter 4). The $CsHSO_4$ was easily dissolving in the methanol solution when placed in the fuel cell.

The MEA preparations included once again the ion conducting $CsHSO_4$, electronic conducting phases, gas diffusion layers and catalyst. The composition was varied to establish the optimum combination of the phases and concentration of the catalyst relative to the electrode composition and membrane requirements. $CsHSO_4$ transforms around 140°C into a superior phase exhibiting a high proton conductivity between 10^{-3} and 10^{-2} S.cm^{-1}.

There were low current densities recorded during testing and the membrane was observed to be unstable in the presence of water or hydrogen (see equation 1). Melting of $CsHSO_4$ takes place around 212°C. In the case of water, the membrane dissolved and perished between the two electrodes. In the presence of hydrogen, the membrane degraded with H_2S release (see equation 1). The evidence (see equation 1) shows that degradation does not necessarily occur in the presence of hydrogen but is mainly due to presence of absorbed water and volatile impurities. This is a worrying factor since methanol (Analytical grade, 99.9 %) is introduced which is volatile and contains a small amount of water. The catalyst used was 40% Pt/C. The platinum catalyst catalyses the decomposition reaction of $CsHSO_4$ and lowers the temperature of decomposition (see equation 1).

4.6 CONDUCTIVITY ANALYSIS – THERMAL DEPENDENCE

The anode and cathode were supported on carbon cloth type 494c 10% PTFE.

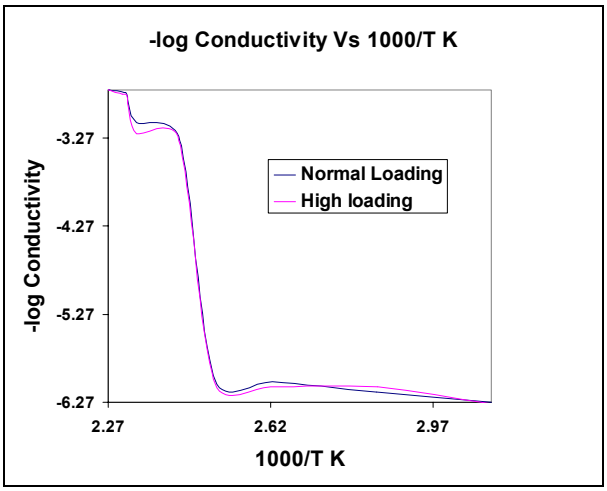

Figure 4.4: Electrodes with normal and high catalyst loading relative to conductivity.

The catalyst loading was increased two fold to investigate the influence catalyst loading would have on the thermally dependent conductivity.

With an increase in catalyst loading there is no significant influence on the conductivity with the previously recorded phase transition and superionic membrane properties displaying similar results. As previously observed the phase transition temperature occurs at approximately 140°C where the ionic conductivity increases considerably. There is a noticeable Arrhenius type plot with the last 4 readings dropping slightly possibly due to external heating errors or instability of the experimental set-up relating to thermal conductivity and insulation. The membrane electrode assembly appeared visibly intact after the experiment with the white of the membrane sandwiched between the black carbon cloth electrodes 494c 10% PTFE. During closer investigation, after the removal of the electrodes, the proton conductor was evidently eroded by either the water presence or adsorption by the membrane or fuel directly involved in the degradation process. Approximately 60% of the membrane electrode assembly mass had eroded and this only after 1hour continuous testing in the fuel cell at temperatures reaching 170°C (443K).

The membrane electrode assemblies were more than a month old and had become perished especially the solid electrolyte. Visual inspection revealed that the once solid electrolyte had dissolved and perished between the two electrodes. New electrolytes were prepared with thicker and denser $CsHSO_4$ content.

The size fitting of the MEA seems fine with the original dimensions i.e. 2.5x2.5 cm (cathode) and 3.0x3.0 cm (anode). The cathode fits perfectly into the rubber O- ring and the O – ring presses against the electrolyte firmly pressing the anode against the flow field.

The membrane was 50% $CsHSO_4$ dried and crystallized on glass fibre filter paper.

The temperature at which membrane and electrodes were pressed together was 142°C.

CHAPTER 5

5. Composite Membrane Formation with Cesium Hydrogen Sulphate

The proton conducting membranes that were prepared with the crystal formation on filter paper method was not mechanically supportive of the reaction conditions that took place at the electrode surface and flow field. The $CsHSO_4$ was easily dissolved in the water and experienced degradation in the presence of hydrogen. The introduction of PTFE with attractive mechanical properties, where PTFE is generally unaffected by water and most organic solvents resulted in more mechanically durable membranes under testing conditions. These properties allow PTFE to fill many applications especially as filler in composites contributing to the mechanical strength of the composite. The introduction of silica serves to increase the surface area and forms a stabilizing platform for the proton conductor when it reaches the super-ionic proton-conducting phase above 230°C (503K). Silica also contributes to the conductivity of the composite [59]. The conductivity-composition relationship determined by the optimum composition that allows for continuous and maximum conductivity, is studied. In each case the constituents were varied depending on the volume fraction of each component and its contribution to the effective functioning of the membrane in respect of mechanical stability and increased conductivity. The frequency response analysis shows a maximum conductivity for each composite attributed to percolation thresholds. The mobile protonic species could possibly be H^+ (H_3O^+).

5.1 COMPOSITE FORMATION : PERCOLATION AND GENERAL EFFECTIVE MEDIA CONCEPTS AFFECTING CONDUCTIVITY

There is an increase in conductivity (σ) as the volume fraction of the conducting phase (ϕ) increases as with typical percolation systems. Once a certain concentration-

conducting phase is reached a significant increase in conductivity at that moment indicates the critical percolation threshold ϕ_c had been reached. A gradual increase in conductivity was observed as the conducting phase is increased until ϕ=1. For high temperature conductivity the ϕ_c lies between 0-0.20 (0-20% conductive phase $CsHSO_4$) [53]. Data recorded here are representative of composites exceeding the accepted (0.4) critical volume fraction, which ensures percolation ($\phi > \phi_c$). This is equated as

$$\sigma_m = \sigma_c [(\phi - \phi_c)/(1 - \phi_c)]^t \qquad [\phi > \phi_c] \quad \text{.....Equation 5.1}$$

where, σ_m is the measured conductivity ($S.cm^{-1}$); σ_c is the conductivity of the conductive phase ($S.cm^{-1}$) and t is the percolation exponent. Whether there is polychromatic percolation with more than two species occupying the lattice sites, a continuum is observed above 20% volume fraction of the conducting phase. Depending on the shape of the conducting particle of $CsHSO_4$, the average number of contacts per grain is 1.5 [54]. This would be applicable to the data recorded here as SEM indicates that the $CsHSO_4$ particles are in contact with its neighbouring agglomeration of $CsHSO_4$ particles. SEM images depicting amorphous composites with granular agglomerations of SiO_2 together with PTFE having insulator properties partially encapsulating the conducting $CsHSO_4$ phase, is 20% insulator by volume fraction. Where the probability of percolation is in the confidence interval and continuous pathways for ion conduction are evident, the t values should be in the region of the universally accepted range. With the ion-conducting phase at 80% of the total composition volume fraction 0.8 the calculated t value is 2.4 and the conductivity of the $CsHSO_4$ is 10^{-2} S/cm. In this case of universal contact between the conducting particles the minimum volume fraction to ensure percolation as critical for $CsHSO_4$ was calculated at 0.4. The lack of continuous paths for the ion

conduction was not significant as the conducting phase was always in excess of 50% in the composites.

5.2 Characterization of the Cesium Hydrogen Sulphate Composites - SEM Images

5.2.1 Membrane A

The composition of the membrane is 80% $CsHSO_4$, 3% SiO_2 and 17% PTFE pressed together to form a solid acid membrane composite. Membrane was 2 mm thick with 1 mm between the electrodes. It had a 46 cm diameter and weighed 7.2 g.

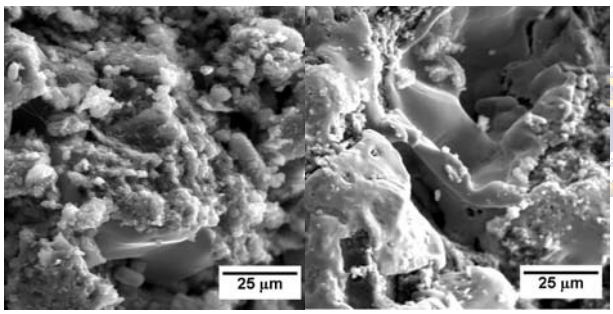

(a) (b)

Figure 5.1 (a-b): SEM images of composite membrane A containing 80% $CsHSO_4$ crystals synthesized with Cs_2CO_3 as the precursor.

Scanning electron microscope membrane images depicted in figure 5.1a and figure 5.1b both have the composition 80% $CsHSO_4$, 3% SiO_2 and 17% PTFE. Figure 5.1b had not been heated prior to SEM analysis at 3000 X magnification. Figure 5.1a is the SEM image, side view of the membrane at a 2000 X magnification. The membrane has also run a complete heating cycle in FRA and the highest temperature reached was a 444 K. Prior to SEM analysis the membrane underwent FRA to 444 K (171°C) to determine the thermal dependence of the phase transition to a super-ionic conductor.

The composition of the membrane is 80% $CsHSO_4$, 3% SiO_2 and 17% PTFE compacted together to form a solid acid membrane composite.

Membrane B

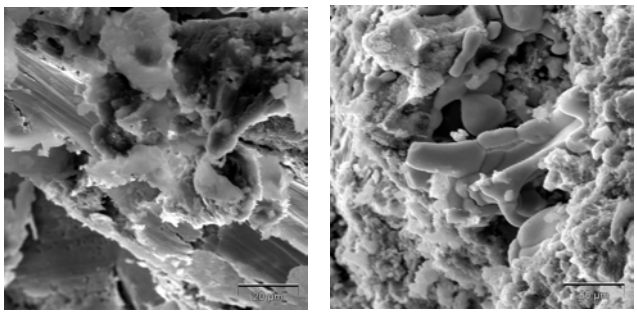

(a) (b)

Figure 5.2 (a-b): SEM images of composite membrane B containing 60% $CsHSO_4$ crystals synthesized with Cs_2CO_3 as the precursor.

Figure 5.2a is the SEM image, side view of the membrane at a 1000 X magnification that has not run a complete heating cycle thus the image is still hydrated. Figure 5.2b has run a heating cycle and is a side view of the membrane C at 1000 X magnification after heating and cooling. Similar to membrane A, membrane B has undergone a thermal cycle while testing the resistance in FRA and the highest temperature reached was at 444 K. Membrane B is composed of CsHSO4, PTFE and SiO_2. From the SEM pictures, there is a visible difference in the appearance of the composite with a more granular structure when heated as opposed to the smooth amorphous appearance of the hydrated specimen in figure 5.2a.

Membrane C

This composite has the composition 53% $CsHSO_4$, 40% PTFE and 7% SiO_2.

The constituents were pressed together at a pressure of 400 bars for 3 minutes at room temperature. The membrane was 2 mm thick and 1 mm thick between the electrodes, 46 cm diameter and weighed 8.4 g.

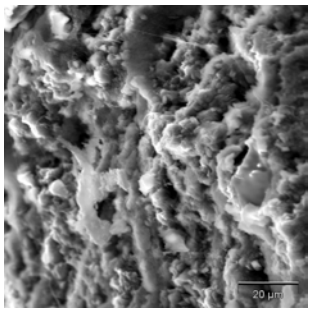

(a)

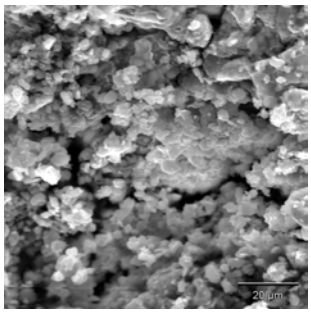

(b)

Figure 5.3 (a-b): SEM images of composite membrane C containing 53% $CsHSO_4$ crystals synthesized with Cs_2CO_3 as the precursor.

Figure 5.3a, which has not run a complete heating cycle (and thus the image is that of a hydrated form) is a side view of the membrane at a 1000 X magnification.

Having undergone a heating cycle figure 5.3b shows a side view of the membrane at 1000 X magnification after heating and cooling. The term "heating cycle" means that the membrane has been heated while testing the resistance in FRA and the highest temperature reached was 444 K. Both membranes in the SEM images 5.3a and 5.3b have similar compositions as mentioned above. From the SEM images, there is a visible difference in the appearance of the composite with a more granular structure when heated above 405K to the super-ionic conductive phase. Water loss and other solvents causing the void-like porous appearance could cause the formation of the porous structure.

Membrane D

Membrane D was prepared the pressing together of the following components, 57,5% volume fraction $CsHSO_4$, 36,5% PTFE and 6,0% SiO_2. This was performed at room temperature and the force applied for 3 minutes. The membrane was 2mm thick, 46cm in diameter and weighed 7.5g.

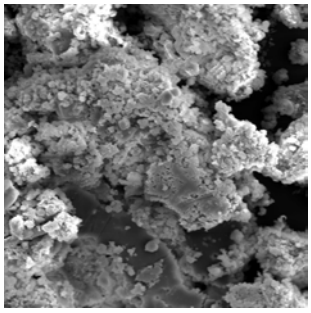

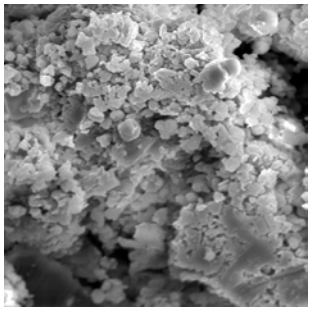

(a) (b)

Figure 5.4 (a-b): SEM images of composite membrane D containing 57.5% $CsHSO_4$ crystals synthesized with Cs_2CO_3 as the precursor.

Figure 4a shows a membrane that has run a complete heating cycle and is a side view at a 500 X magnification.

Figure 5.4b shows a side view of the membrane at 1000 X magnification. The membrane has also run a complete heating cycle in FRA and the highest temperature reached was a 444 K. The composition of both membranes is 57,5% $CsHSO_4$, 36,5% PTFE and 6% SiO_2.

Membrane E

Preparation:

Composition: 60% $CsHSO_4$ and 40% PTFE and pressed at 400 bars for 3 minutes

Properties of membrane E: 2 mm thick, 46 cm diameter and 7 g.

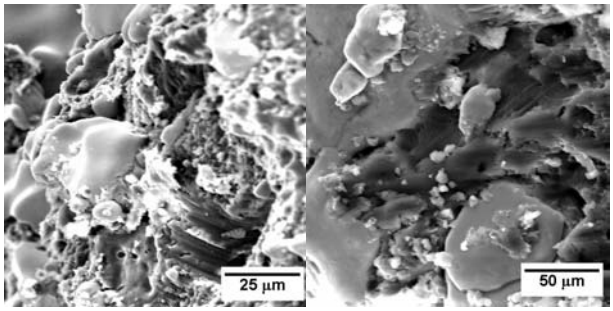

(a) (b)

Figure 5.5 (a-b): SEM images of composite membrane E containing 60% $CsHSO_4$ crystals synthesized with Cs_2CO_3 as the precursor.

In figures 5.4a and 5.4b, the membrane has not run a complete heating cycle. Figure 5a shows a side view of the membrane at a 1000 X. Figure 5.4b shows a side view of the membrane at 500X.

Membrane F

Membrane F was composed of 70%$CsHSO_4$, 30%PTFE. The membrane was 2mm thick, with a 46cm diameter and weighed 7.5g.

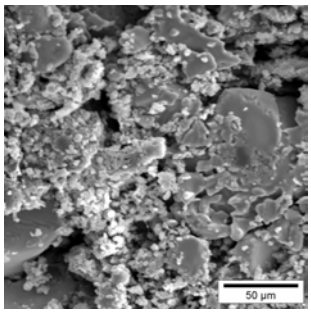

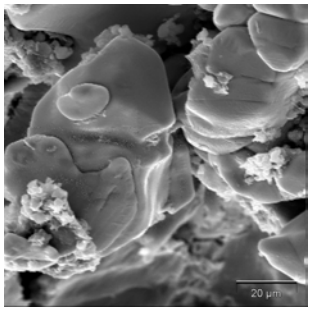

(a) (b)

Figure 5.6 (a-b): SEM images of composite membrane F containing 70% $CsHSO_4$ crystals synthesized with Cs_2CO_3 as the precursor.

Figures 5.6a and 5.6b are side views at 500 X and 1000 X magnification respectively. Neither has run a complete thermal cycle.

Membrane G

Membrane G was composed of 50%$CsHSO_4$ and 50%PTFE. The membrane was 2 mm thick with a 1 mm thickness between the electrodes, 46 cm diameter and weighed 7.5 g.

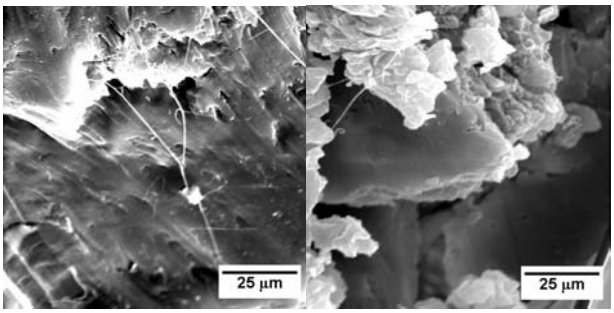

(a) (b)

Figure 5.7 (a-b): SEM images of composite membrane G containing 70% $CsHSO_4$ crystals synthesized with Cs_2CO_3 as the precursor.

The images are those depicting the membrane prior to heating. Figure 7a is a side view at 2000 X and 3000 X magnification.

Membrane H

Membrane H was prepared with the composition 90% $CsHSO_4$ and 10% PTFE. It was 2 mm thick and 1 mm thick between the electrodes, 46 cm diameter and weighed 7.5 g.

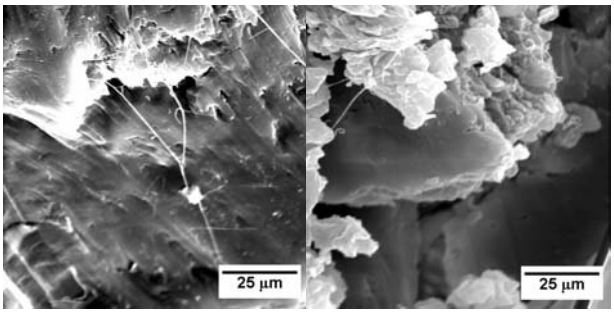

(a) (b)

Figure 5.8 (a-b): SEM images of composite membrane H containing 90% $CsHSO_4$ crystals synthesized with Cs_2CO_3 as the precursor.

The membrane in figures 5.8a and 5.8b at 500 X and 1000 X magnification respectively, have not run a complete heating cycle.

Composition: 90% $CsHSO_4$ and 10%PTFE.

5.3 INFRARED SPECTROSCOPY (IR) TO CHARACTERIZE THE COMPOSITES

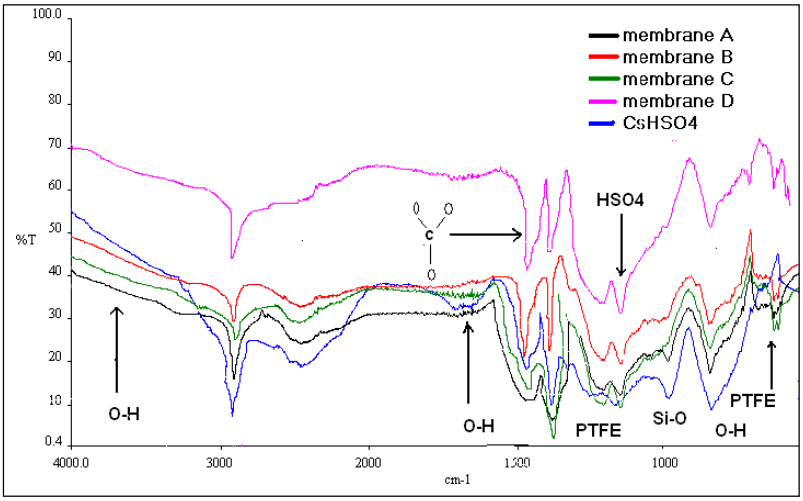

Figure 5.9: IR spectral analysis comparing different compositions.

<u>Membrane A at 353K</u>

Sulfates have strong bands in the region 1080 to 1150 cm^{-1} and also a medium strong band between 580 and 670cm^{-1}. There are very small or no differences in the structure after heating to 80°C (353K). The sulphate band region includes peaks of similar resolution and strength to those analysed at room temperature. Hydroxyl bands typical in the region 3700 – 3100cm^{-1} are absent. This indicates possible water or solvent residue loss on drying at low temperature. Slight peaks between 1410 and 1450cm^{-1} suggest the incomplete conversion of Cs_2CO_3 in the presence of H_2SO_4 to Cs_2SO_4, as this band area is indicative of carbonates (CO_3^{-2}). The heating rate was

gradual and no visible change to the membrane surface was observed. Membranes A, B, C and D with $CsHSO_4$ were also viewed by the higher magnification 'zoom in' feature to observe the infrared peaks in greater detail.

4. Membrane A at 378K

After heating membrane A to 105°C (378K) the peaks seem sharper and more defined. The structure has not changed but the loss of water and other solvents has enhanced the resolution compared to the infrared analysis at room temperature.

$CsHSO_4$ and PTFE Composites

Composites containing $CsHSO_4$ and PTFE were prepared to investigate the mechanical and conductivity dependence on thermal influences and served as an isolation technique to identify the band regions for SiO_2 peaks which would obviously be absent in the $CsHSO_4$-PTFE composites and only present in the $CsHSO_4$-PTFE-SiO_2 composite. The thermal stability of the composites was thus investigated by observing the change in structure using infrared analysis. These were membranes E, F, G and H containing varying volume fractions of PTFE.

For the tri-component composites namely membranes A, B, C, and D have a band region 1100 – 1300 cm^{-1} with two peaks indicative of polymer presence. This is further substantiated by membranes F and G where the 70 and 50% PTFE respective fractional percentage clearly shows distinct and defined peaks in the 1100 – 1300 cm^{-1} band width region. These peaks are not observed in the pure $CsHSO_4$ spectrum. The presence of PTFE contributes to the diminished size of the water band. SiO_2 has the opposite effect by increasing the size of the water band when the SiO_2 fractional percentage is increased. The definition of the peak increases as the fractional composition of the SiO_2 in the composite increases along with $CsHSO_4$

Between 700 and 1250 cm^{-1}, the silica species may be observed. Specifically Si – O bond stretching is found in the range 700 – 1100 cm^{-1} but this peak is also present in composites where SiO_2 is absent. Therefore SO_4 bonds may be represented by the identified peaks. [49,50].

The structure seems very stable with predictable changes in structure depicted in the transmittance infrared diagrams with varying compositions. The fractional composition is clearly seen with the trend in the size of the peaks, which are proportional to the concentration of the different components. The series of thermal cycles performed on the membranes have no significant effect on the structure of the individual components in the composite. Similar trends in the infrared spectroscopic analysis are observed in samples that have undergone thermal cycles as compared to those that have not been subjected to the FRA. FRA was performed simultaneously with thermal cycling.

5.4 AUSTERITY AND STABILITY TESTING

5.4.1 pH Determination to Establish the Stability of the Composite Influencing the Frequency Response Analysis Causing Drift

The pure $CsHSO_4$, which is soluble in water and dilute methanol (1M), has a pH of 4. The pH was measured when the solution was at room temperature. A 0.1% solution sample was used. The process by which the pH was measured included varying the temperature and thereafter bringing the solution temperature back to room temperature once the reaction between the membrane and water has taken place. This showed the influence if any, of the thermal effect on the degradation of the membrane with the subsequent release of protons into solution. Membrane composites with 0.8

volume fraction $CsHSO_4$ and 17% PTFE, showed a greater dissolution in the dilute 1M methanol with up to 30% of the solid membrane dissolving at room temperature; whereas a membrane with a volume fraction of 34% PTFE content experienced 19% dissolution at similar temperatures. In both instances the stirring rate was 300 rpm. For the membrane with 17% volume fraction PTFE, the pH change was not significant within the first hour of continuous stirring.

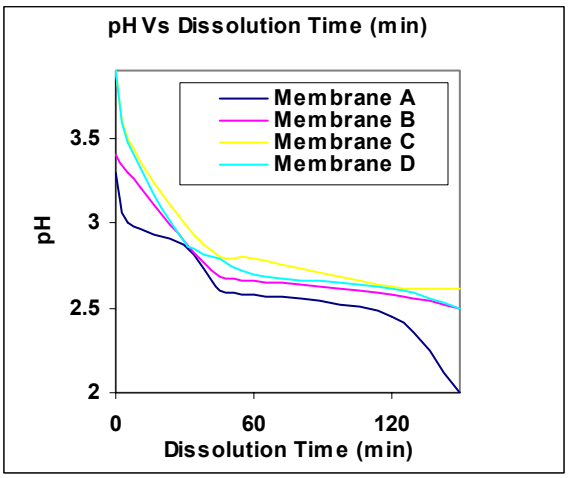

Figure 5.10: The pH and dissolution time relationship.

Composites containing a higher volume fraction PTFE do not dissolve as easily as those with a lower PTFE content. This is evident in membrane A with 17 wt% PTFE and membrane C with 40 wt% PTFE.

5.4.2 Hydrogen gas causes degradation of the membrane and the stability of the Composite

The composites were exposed to hydrogen gas for varying periods of time. The degradation rate was recorded over time by weighing the composites at different intervals.

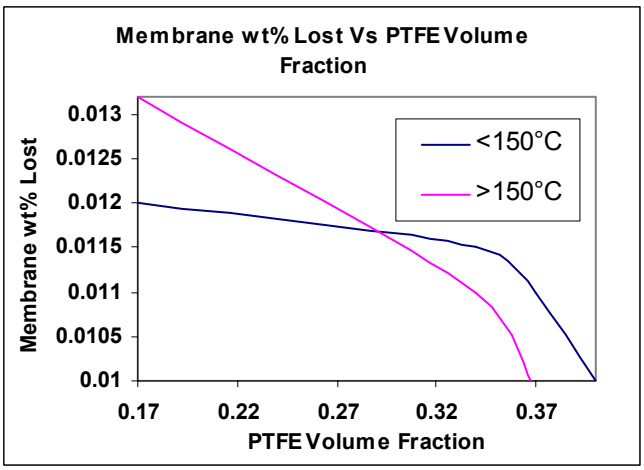

Figure 5.11: The relationship between the membrane wt% lost and PTFE volume fraction.

Once again the composites containing the higher concentrations of PTFE were not as easily degraded. The reaction

$2CsHSO_4 + 4H_2 \rightarrow Cs_2SO_4 + H_2S + 4H_2O$

outlines the degradation of cesium hydrogen sulphate and formation of hydrogen sulphide gas. The evidence suggests the minimizing of the degradation process as the PTFE concentration is increased. Temperatures above 423K where the super-ionic phase already reached could possibly encourage the formation of hydrogen sulphide and thus the instability of the membranes. The unstable membrane could enhance the conductivity by adopting the semi-crystalline ionic structure. The volume fraction of the insulator substance reduces the conductivity as previously recorded when the

concentration thereof is increased. There was a significant difference in mass lost due to temperatures above 423K.

5.5 Conductivity Analysis

5.5.1 Ahrrenius Representation of Thermal Dependence Conductivity

The heat and water effect on the conductivity is clearly illustrated in the graph below.

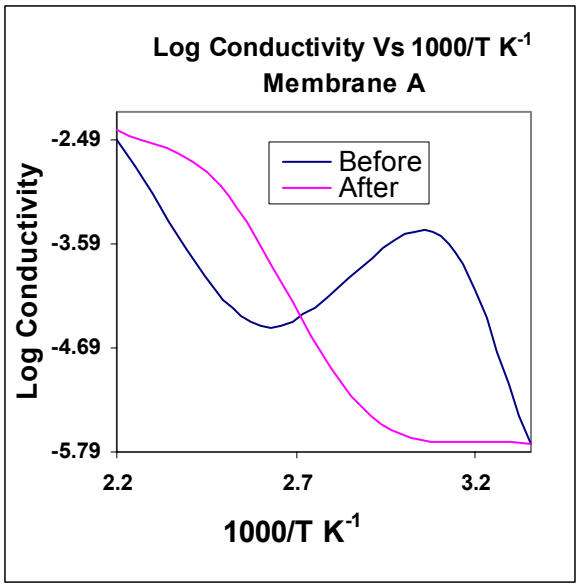

Figure 5.12: Temperature dependence of conductivity, (σ, $S.cm^{-1}$), up to 453K.

The resulting graph indicates possible dehydration since the membrane lost water during heating. The conductivity showed an increase at first until the water was lost followed by a decline in conductivity until the super-ionic conductivity phase was reached at around 132°C (405K) where the conductivity increased significantly.

Membrane A was retested after 3 days at room temperature, unprotected from moisture. The graph (fig. 5.2) resembled that of the first cycle suggesting the water loss was not replenished possibly due to the presence of the insulator properties of PTFE. Membrane B was tested under thermal dependence conductivity conditions by

heating to approximately 180 °C (453K) and allowing to cool before repeating the thermal conductivity test analysis.

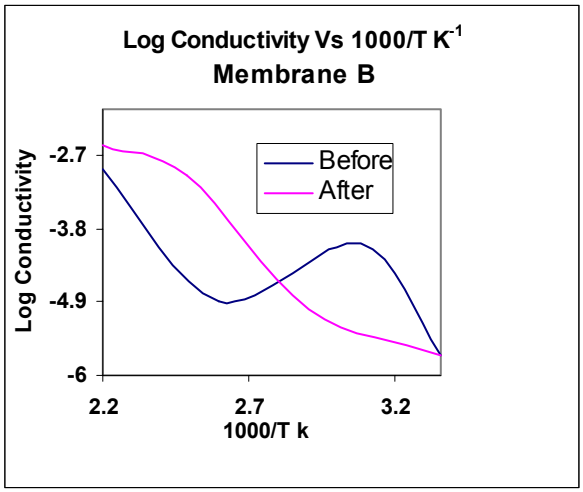

Figure 5.13: Membrane B thermal dependence conductivity, σ, $S.cm^{-1}$, before and after heating.

Membrane A water content due to its high salt content at 0,8 volume fraction as opposed to 0,6 volume fraction for membrane B, could explain the higher conductivity seen at room temperature after the first session of testing. This increase at lower temperatures (approximately 52 °C (325K)) is soon lowered as the water is lost due to further increase in temperature above 60 °C (333K). The membrane was able to prevent water absorption over 2 days, possibly due to the PTFE content. The conductivity was noted to be lower than that of membrane A. The next phase transition relative to temperature increase occurs at 112 °C (385K) where the solid acid electrolyte that by now is dry on the surface, becomes an ionic conductor. A further increase in temperature (approximately 132 °C (405K)) the membrane reaches a super-ionic conductor state. The phase transition temperature and structure changes are recorded as body centered cubic to monoclinic.

Phase Determination by Structural Changes during External Treatment – Heating. Previous results show the effects of temperature as a function of structural changes

the membranes undergo during the heating and cooling cycles [45]. Samples that were heated from 25 to 140°C and cooled back to 25°C confirmed the presence of the low and high temperature phase transitions. The powder diffraction patterns measured between room temperature and 100°C were similar to the calculated pattern for $Cs_3(HSO_4)_2(H_2PO_4)$. Also present were a few Cs_2SO_4 peaks. As established previously, the phase transition starts to take place around 108°C (381K). As the temperature increases, the monoclinic peaks initially become weaker until they completely disappear at around 132 °C (405K). Conductivity measurements support the temperature range for the above-mentioned phase transition of 111 to 125°C. Visual inspection of the crystals after a complete thermal cycle of heating and cooling, show the crystals transforming from clear to milky white crystals further supporting the occurrence of macroscopic structural damage data.

The diffraction patterns, which were obtained at 140°C [57,58], show that the super-ionic phase is body-centred cubic with a lattice constant of 6.961 Angstroms. The monoclinic to body-centred cubic phase change accompanied by the structural change was further supported by differential scanning calometry (DSC) measurements. A relationship is observed between the X-ray measurements and lower phase transition temperature when doping with inert oxides is applied to the composites. The phase change exhibits a heat of transformation of 40 J/g (Joules/gram). The slight difference in the heat of transformation from normal to super-ionic conductive properties is reflected in the temperature (approximately 140 °C (413K)) and can be very significant in explaining the phenomena. Conductivity results have lower temperature phase change readings as compared to the DSC measurements. Those of X-ray measurements, in relation to having similar phase transition temperatures, further support conductivity results that are higher than calorimetric methods of

detection. During the cooling down period there was an absence of information to show transitional changes. This could be explained by the common occurrence of slow transitions resulting in even slower transformations too slow to be detected by calorimetric methods.

Sulphate Hydrogen bonding: For $CsHSO_4$ there is one proton for each sulphate group, thus, in a structure in which all sites are occupied, only two oxygen atoms can be hydrogen bonded per sulphate tetrahedron. These are possible configurations, occurring at low temperatures as chains and possibly dimers [57,58]. In the super-protonic phase the sulphate tetrahedra undergo rapid reorientations and both the oxygen atoms and the protons are distributed over four times as many crystallographic sites as there are species [58]. By adopting this disordered structure, the compound permits every oxygen atom to be hydrogen bonded. This evidently suggests that entropic considerations, which favour chemically similar or even equivalent S-OH bonds, steer the transition into a disordered state. The nature of this disordered state gives rise to high conductivity [55].

SiO_2 pore sizes: The localization of alkali metal hydrogen sulphates in the pores of the SiO_2 matrix causes the stabilization of different disordered states depending on pore sizes. For composites with pore sizes 35-70 Angstroms, considerable changes in transport, structural and thermodynamic properties are observed with amorphization of $CsHSO_4$. Data similar to these observations mentioned above include unusual properties of clusters, thin films and substances confined to small pores of solids. In this work temperature conductivity dependence using approximately 60 wt% $CsHSO_4$ and 40 wt% SiO_2 composition were analysed using a specific surface area (500 m^2/g) SiO_2 and varied pore sizes (14 and 35 Angstroms). As supported in other literature sources the addition of SiO_2 increased the conductivity of the low

temperature phase and decreased the conductivity of the high temperature phase. The conductivity of the composites based on various types of silica, differs essentially in the low temperature conductivity of the composites when using silica with the pore sizes 35 Angstroms. This is also one order of magnitude higher than the conductivity when using silica of pore size 14 Angstroms. Where similar research had taken place with varying silica types, essentially provided information about the properties to be considered when composites are formed which need not include surface area as of primary importance but also depends on the character of the heterogeneous dopant porous structure, particularly the pore radius which most importantly should be taken into account [59]. With varying volume fractions of $CsHSO_4$ and SiO_2 once again with different SiO_2 pore sizes (70 and 170 Angstroms), the dependencies differ markedly with both the volume fraction and the pore sizes. The phase transition temperature of composites using the 70 Angstroms pore radius decreases significantly (ca 20K) as the volume fraction of silica increases. A simultaneous drop in the conductivity is observed with, and practically disappears, as the volume fraction of SiO_2 becomes less than 0,6. Conductivity depends significantly on an increasing silica volume fraction and increases by more than two orders of magnitude for the low temperature phase, whereas for the high temperature phase, conductivity of $CsHSO_4$ in the composite decreases with an increasing silica volume fraction. The activation energy of the low-temperature conductivity in the composite is 57,8 ± 4,8 kJ/mol. Similar dependencies with close conductivity values and activation energy are observed for composites with silica pore size of 35 Angstroms. Conductivity dependencies on silica with pore sizes of 14 and 1000 Angstroms in composites, are similar to that of the pure $CsHSO_4$, and maximum conductivity values are 6-8 fold higher than that of the pure salt. Composites with silica pore size of 170 Angstroms

have displayed some extraordinary behaviour, where the super-ionic phase transition becomes more diffuse as the volume fraction of silica is increased. Simultaneously the phase transition temperature of $CsHSO_4$ in the composite decreases significantly for instance, for the temperature at 350K and the 0,7 silica volume fraction. Data at low temperatures indicate the activation energy at 91,5 ± 4,8 kJ/mol, which is higher than that of silica based composites with silica pore sizes of 35 and 70 Angstroms [32, 48, 60].

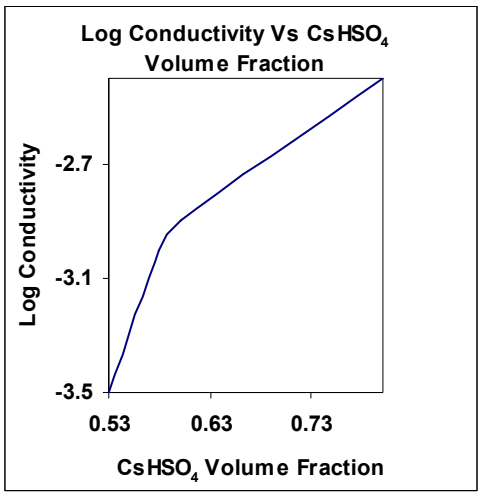

Figure 5.14: Log Conductivity, σ, $S.cm^{-1}$ relative to the $CsHSO_4$ Volume fraction.

The conductivity was recorded at approximately 180°C (453K). Percolation is dependent on the quantity of conducting material in the composite. This implies the t values are in the universal region and that the conduction process is dominated by contact processes. The number of contact sites per conducting grain exceeds 1,5. This could be further supported by the silica presence that stabilizes the composite and increases the surface area.

5.5.2 Proton Conductivity Determination by Frequency Response Analysis (FRA) and Fitting Data to Equivalent Circuit Models

The frequency response analysis results could be affected by factors that compromise the steady state of the electrochemical impedance system. Drift is a common cause of this problem. The cell itself could have altered through adsorption of impurities on the surface of the electrolyte, formation of an oxide layer, build-up of reaction products between the electrode and electrolyte, surface degradation of the electrolyte and temperature changes. To counter the problem of instability, thermal cycles were employed to ensure consistency of results. The recorded data was displayed graphically. Nyquist plots are used to show the resistance at various temperatures in Z' and Z'' form as parametric functions of frequency.

Membrane A
Before the super-ionic phase

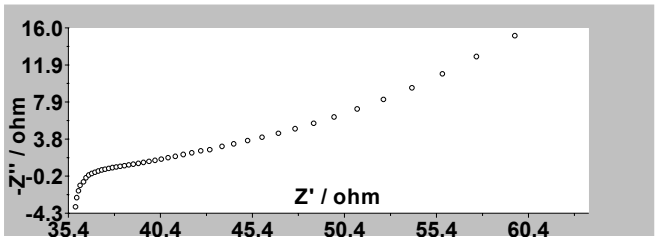

Figure 5.15: Nyquist plots before the super-protonic phase transition.

For the composite membrane A with 80% conducting phase $CsHSO_4$, the insulating non-conducting phase is composed of 17% PTFE and 3% SiO_2. This composite has a semi-circular type appearance with the number of semi-circles specific to the properties of the composite components.

The representation for the infinite Warburg impedance on a Nyquist plot appears as a diagonal line with a slope of 0.5. The Warburg impedance is visibly affected by temperature. After the super-ionic phase temperature is reached there is a difference in the solid electrolyte phase.

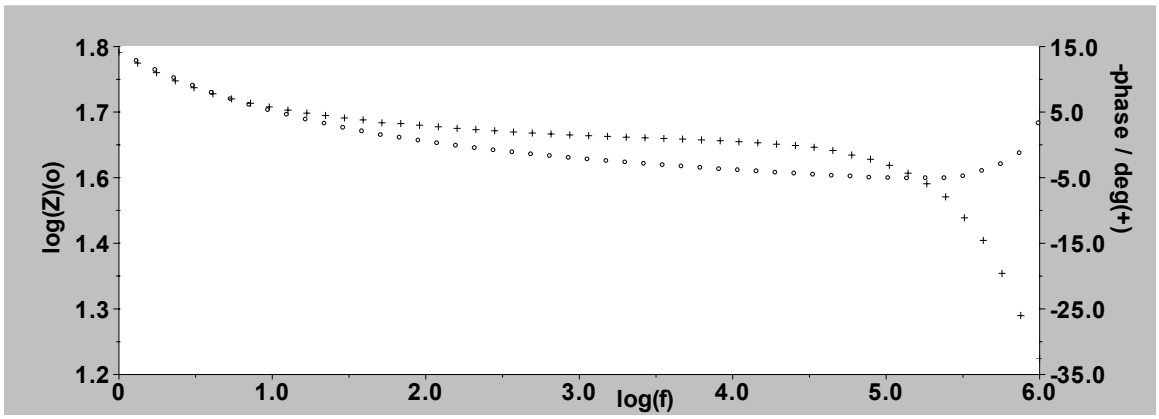

Figure 5.16: Bode plots before the super-protonic phase transition.

The impedance goes up but capacitance goes down when capacitors are connected in series. This is a consequence of the inverse relationship between capacitance and impedance. Impedance is created by the diffusion. Impedance created by diffusion is known as Warburg impedance. The resulting impedance is subject to the frequency of the potential perturbation. The data represented here suggests that at high frequencies, low impedance are encountered only from 10^5 Hz, which increases gradually as the frequency is lowered. This applies to the Warburg impedance as well, with low impedances at high frequencies increased impedance as the frequency is lowered. This observation is explained by the distance the diffusing species have to move-where short distances are analogous with high frequencies and longer distances with low frequencies, thereby increasing the Warburg impedance. On the Bode plot the Warburg impedance exhibits a phase shift of 45°.

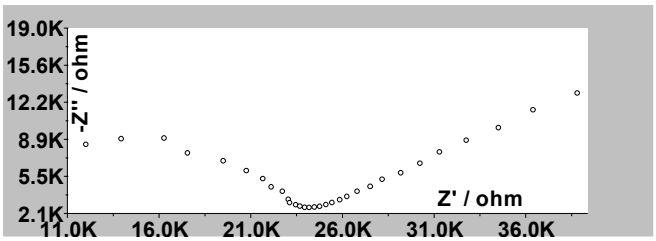

Figure 5.17: Typical Nyquist plots after the super-protonic phase transition.

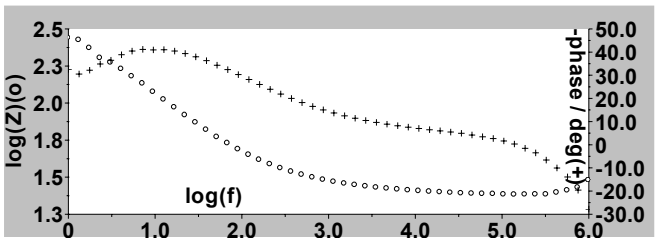

Figure 5.18: Typical Bode plots after the super-protonic phase transition, where + refers to the phase and o, the impedance .

During the conductivity measurements the temperature was kept constant or changed stepwise. The conductivity of each sample was determined from the frequency dependence of the real and imaginary part of the impedance plotted in the complex plane (Cole-Cole plot)[6].

The focus was on the removal of absorbed water in all forms. As depicted, in the Ahrrenius plot thermal cycles, [fig. 5.12 and 5.13], when cooling, the conductivity was much higher than the initial conductivity when heating. With the use of PTFE as a hydrophobic insulator adding to the mechanical strength of the membrane, water re-absorption after removal was minimal. The conductivities were determined at the 80, 60, 53, and 58% $CsHSO_4$ volume fraction of the composite. This was graphically displayed in Arrhenius form [fig. 5.14]. The results indicate that the super-ionic phase, the $CsHSO_4$ in the membrane, undergoes a phase change resulting in elevated conductivity at 403 – 418K. This phase is observed in similar temperature regions for each composite and that of pure $CsHSO_4$, suggesting that PTFE polymer presence had no effect on the transition temperature. With the addition of SiO_2 previously heated to 1173K, the conductivity increases at lower temperatures as supported in the

literature [30,33]. Although the 3% SiO_2 volume fraction is a small component of the composite, lower temperatures are experienced when compared to pure $CsHSO_4$. The heterogeneous doping has a positive effect on the $CsHSO_4$ as an ion conductor, reaching the phase transition and enthalpy of formation at lower temperatures.

At the lower temperatures of 353K (80°C), Nafion reigns supreme with high conductivity in the hydrated form, but at higher temperatures above 363K (90°C) dehydration causes loss of conductivity [51, 52]. With the addition of SiO_2 in the composite as stabilizing agent at high temperatures, which is also an insulator, there was a notable increase in conductivity. For composites of this nature the macroscopic conductivity relies on the conductivity of the individual components, volume fractions and spatial distributions [53].

5.5.3 Test Conditions and Influence of Sample Treatment on Conductivity and the Frequency Response Analysis

The test conditions influenced the conductivity where the mesh was omitted an increase in resistance was observed which tends to emphasize the importance of the contact between the electrode and housing to which the small current potential is transferred to allow the controlled frequency to reach the capacitor between the electrodes. Supplying an alternating current potential to the cell and measuring the current through the cell, measures the electrochemical impedance in this case. The metal mesh is stainless steel and itself has a resistance of 0.7 ohms.

The signal processing domains refers to data domains. The same data is represented in different domains namely, time and frequency domains. The capacitor impedance decreases as frequency is raised. At high frequency there is a lower impedance and gradual increase in impedance as the frequency is lowered.

Impedance increases but capacitance goes down when capacitors are connected in series.

Unfortunately most electrochemical cells do not have even or uniform current distribution throughout the electrolyte area.

5.4.3.1 SiO_2 Pre-heating

The SiO_2 was heated to 1173K (900°C) prior to composite formation. The heating procedure when omitted allowed the hygroscopic SiO_2 absorbed water to be trapped in the composite after compression. This was evident in the infrared spectra where the low transmittance indicated high water content. This absorbed water could not be easily removed from the composite by drying at 105-120°C. Heating the membrane above 200°C to release the water caused irreversible damage to the conducting properties of the membrane.

5.4.3.2 Temperature dependence of conductivity

Another important development appears in connection with the temperature dependence of conductivity at 433-473K, which is probably caused by stabilization of the $CsHSO_4$ melting state at lower temperatures. In the high temperature region, the conductivity of all composites with silica volume fractions less than 0.4 changes slightly and correlates with the conductivity of pure salts. As volume fraction of silica increases to approximately 0.8 the high temperature conductivity decreases due to the percolation of the conductor insulator type [32, 48, 60]. When the volume fraction of silica is 0.5 – 0.7 in the composite at low temperatures the conductivity is maximum. The volume fraction corresponds to 30-50 vol.% (volume percentage) of silica in the composite. Similar dependencies were observed for Li^+ and Ag^+ containing composites [48, 61, 62, 63], and protonic composites [30].

5.4.3.3 Temperature and Water Content Influence on Conductivity

Thermal gravimetric analysis revealed that $Cs_3(HSO_4)_2(H_2PO_4)$ starts to decompose at 155°C (428K) via the loss of water. The maximum weight loss occurred in the region of 180°C. The total weight loss of 16.5 wt% is significantly higher than what would be expected based on the stoichiometry of $Cs_3(HSO4)_2(H_2PO_4)$ at 5.2 wt%. Data suggest that this is due to the occasional presence of water within voids in the crystals. Cesium hydrogen sulphate ($CsHSO_4$) crystal growth exhibits similar behaviour when grown from aqueous solutions [56].

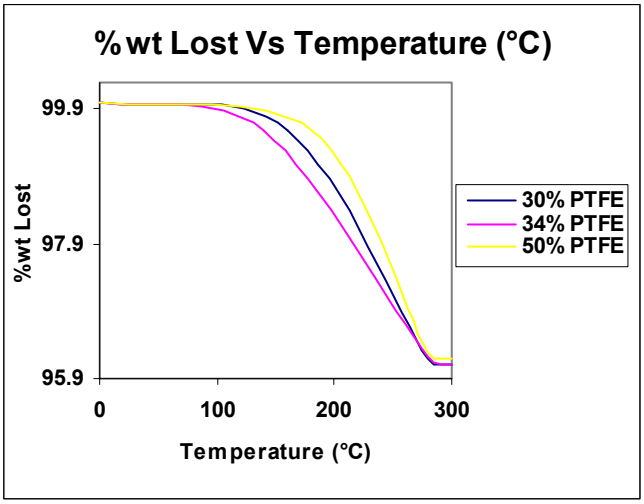

Figure 5.19: TGA of membranes with varying PTFE and SiO_2 content.

The membranes containing a high amount of PTFE, tend to be less susceptible to water loss at high temperatures, and as observed earlier, the membranes containing PTFE absorb less water, if any. Silica content in the membrane containing 34% PTFE offers a different perspective to water loss. The water does not significantly increase the conductivity at high temperatures as the super-ionic phase transition takes place at approximately 132 °C (405K) and the bulk of the water or solvent is lost at around 145 °C (418K) and higher. Data supporting the proposed mechanisms for proton conduction in $CsHSO_4$ studied by quasi-elastic neutron scattering concluded that in

the high conductivity phase the hydrogen bond net work is subjected to permanent reconstruction as the protons change their crystallographic sites. There was also supporting evidence to suggest two types of diffusion where one is a fast reorientation of HSO_4 defects and the other a slower long-range translational proton diffusion. The slow long range translational diffusion is thought to be responsible for the high protonic conductivity. This data was further supported by different methods namely calorimetry, optical and neutron spectroscopy, and NMR [66]. The water content can easily influence the crystallographic component conductivity by either enhancing or lowering translational diffusion by accelerating or slowing down the process. Distances between crystallographic sites are reduced with the assistance of cations, such as H_3O^+ due to water presence.

Particular attention was given to the storage of dried sample used for testing. Desiccators were employed where the base section contained a chemical drying agent, anhydrous calcium chloride (Reagent grade, 99,9%). This precaution of preventing hygroscopic samples from absorbing moisture from the atmosphere was observed more often with CsH_2PO_4 in chapter 6 since CsH_2PO_4 proved to be more hygroscopic than $CsHSO_4$.

CHAPTER 6

6. CsH_2PO_4 (CESIUM DIHYDROGEN PHOSPHATE)

6.1 COMPOSITE FORMATION WITH CsH_2PO_4 (JUSTIFICATION)

The composites containing phosphate have different results to that of sulphate containing composites where the super-protonic transition in a phosphate-containing compound, clearly demonstrates that the chemistry of phosphorus does not prevent such transitions from taking place. Thus the difference between the electrical properties of $CsHSO_4$ and CsH_2PO_4 has to be due to some other facet in the compound. Here the hydrogen bond scheme is examined. In CsH_2PO_4 there are two protons per phosphate, or, alternatively viewed, 4 half protons per phosphate. When at room temperature every oxygen atom can be hydrogen bonded without the introduction of disorder or partial occupancies. Consequently, even if transitions into phases of higher symmetry were to occur at elevated temperatures, we would not expect them to significantly alter the hydrogen bond scheme.

6.2 CHARACTERIZATION OF COMPOSITES BY SEM

6.2.1 Preparation of membrane I included in the composition 50 wt% CsH_2PO_4 and 50 wt% PTFE.

The membrane I was 2 mm thick around the electrodes and 1 mm thick across and in between the electrodes, with a 4.6 cm diameter and weighed 8.0 g. The density was calculated at 2.41 g/ml.

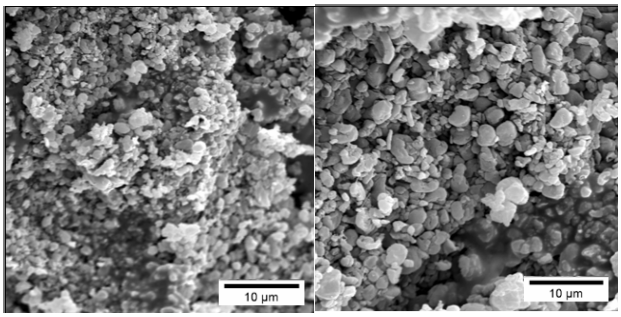

(a) (b)

Figure 6.1 (a-b): SEM images of composite membrane I containing 50 wt% CsH_2PO_4.

Membrane I has not run a complete heating cycle thus contains a fair amount of moisture, as the cesium dihydrogen phosphate is highly hygroscopic. The images reveal the agglomerations of PTFE that does not dissolve or adhere easily to most solvents particularly water. The PTFE powder rejects the slight moisture content in the CsH_2PO_4 and tends to form agglomerations away from the ion conducting salt.

6.2.2 Membrane J

The preparation of the membrane with composition 57 wt% CsH_2PO_4, 43 wt% PTFE was done at room temperature and 400 atm. The membrane was 0.2 cm thick, 4.6 cm diameter and weighed 8.0 g. Calculated density was in the region 2.41 g/ml.

Figure10a 1000X figure 10b 500X

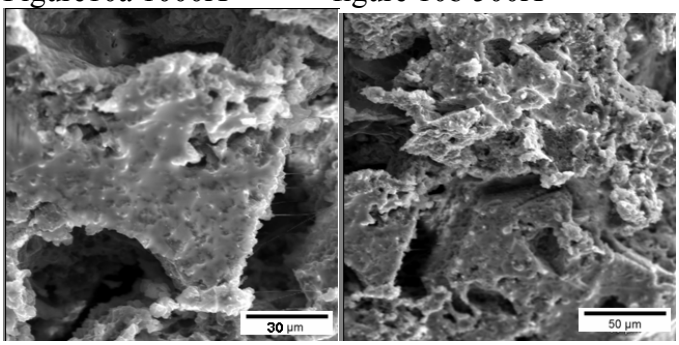

(a) (b)

Figure 6.2 (a-b): SEM images of composite membrane I containing 57 wt% CsH_2PO_4.

The membranes in figure 6.2a at 1000 X magnification and figure 6.2b at 500 X magnification has not run a complete heating cycle. Membrane J had to be heated in the oven because it had been attracting water from the surroundings.

6.2.3 Membrane K

Composition, 65 wt% CsH_2PO_4 and 35 wt% PTFE in composition.

Properties of membrane K: 2 mm thick, 4.6 cm diameter, weight 8.0 g and density of 2.4g/ml.

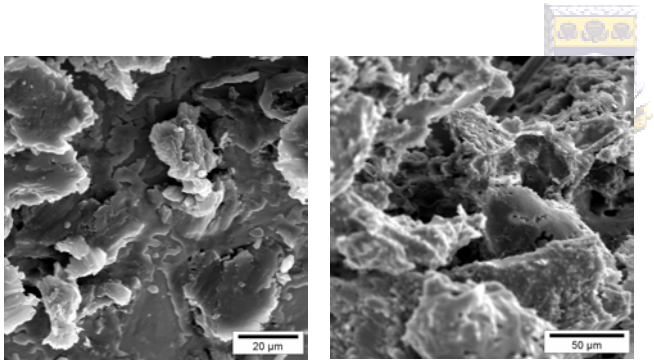

(a) (b)

Figure 6.3 (a-b): SEM images of composite membrane K containing 65 wt% CsH_2PO_4.

Membrane K: both membranes in figure 6.3a at 1000X magnification and 6.3b at 500X magnification have not run a complete heating cycle. Membrane K had to be heated in the oven because it had been attracting water from the surroundings.

6.2.4 Membrane L

Preparation: Composed of 70 wt% CsH_2PO_4, 30 wt% PTFE at room temperature of approximately 25 ^{o}C (298K) and 400 atm pressure. Membrane L was 0.2 cm thick, 4.6 cm diameter and weighed 8.0 g. The density was calculated at 2.41 g/ml.

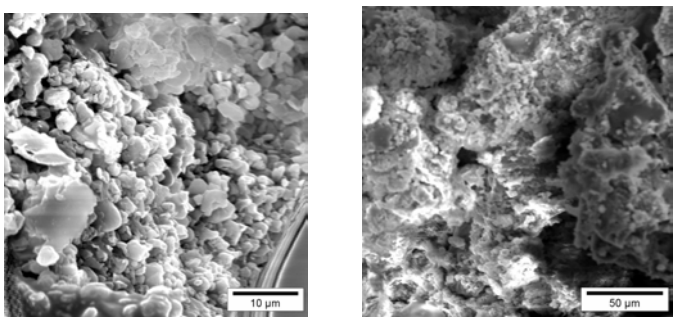

(a) (b)

Figure 6.4 (a-b): SEM images of composite membrane L containing 70 wt% CsH_2PO_4.

Membrane L both membranes in figure 6.4a at 1000 X magnification and figure 6.4b at 500 X magnification have not run a complete heating cycle. Membrane L had to be heated in the oven because it had been attracting water from the surroundings.

6.3 Characterization of composites by IR

Infrared spectroscopy is employed to determine the thermal behaviour on the structure of the proton conducting membrane during operation under intermediate temperature conditions. Sulphates have strong bands in the region 1080 to 1150 cm^{-1} and also a medium strong band between 580 and 670 cm^{-1}. The presence of hydroxyl bands in the area 3700 to 3100 cm^{-1} is convenient for distinguishing the different hydrates. Carbonates all have the strong band around 1410 – 1450 cm^{-1}. They also have a medium

strong band in the 840-880 cm^{-1} range a band which normally goes to lower frequency as the cations become heavier.

6.3.1. Infrared Analysis of Membranes L and H heated to 80°C

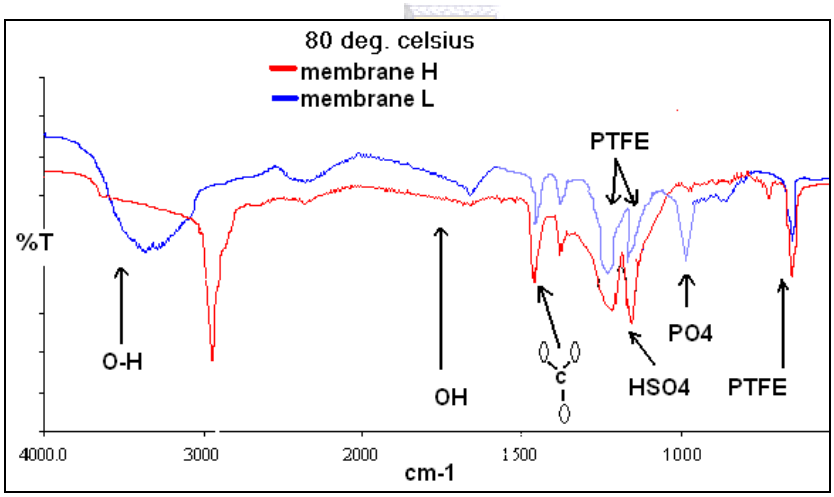

Figure 6.5: Infrared Analysis of Membranes L and H heated to 80°C.

For membranes H and L the ion conducting materials are, $CsHSO_4$ and CsH_2PO_3 respectively. The volume fraction for the ion conducting species is 0,9 for membrane H and 0,7 for membrane L. Membrane H does not have silica as a component in the composite but PTFE as insulator against solvent adsorption, and CsH_2PO_4 as ion conducting material. CsH_2PO_4 is highly hygroscopic when allowed to cool to room temperature but remained dry as the analysis was performed immediately after heating. Strong and polarized bands are found at 772 cm^{-1} and 925 cm^{-1} for

monomeric species corresponding to γSiOH and νSiO^{-1} symmetric stretches [49]. The SiO^{-1} was formed possibly during composite formation and further exposure due to the loss of solvent seen here as small peaks evident in the 880 – 890 cm^{-1} region.

6.2.2 Infrared Analysis of Membranes L and H at room temperature after 18 hours of Cooling

The infrared spectrum produced peaks of poor quality relative to the spectra where the sample was exposed to heat treatment prior to analysis. The peaks were small and unreliable for examination and drawing conclusions. This was due to the level of moisture attracted by the membrane during the cooling stages while exposed to the atmosphere.

The CsH_2PO_4 once again proved hygroscopic when analysed by infrared spectroscopy. The preheating treatment of the composite membrane of different volume fraction insulator and possible waterproofing, could only be viewed at temperatures above 120°C. The impact of the water insolubility properties was viewed once the sample had been heated and allowed to cool. There were no structural changes with respect to the regions of interest that formed part of the integral structure after heating in the absence of water.

6.4 AUSTERITY AND STABILITY TESTING OF COMPOSITES

6.4.1 Stability testing for the dissolution period in water at varying temperatures

The membrane was subjected to stability testing for six hours to determine the mass lost due to dissolution in water at room temperature. The salt content in the membranes was not stable with less than 50 wt% PTFE volume fractions.

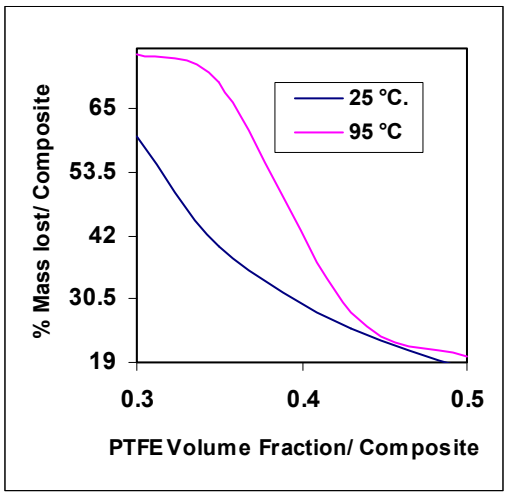

Figure 6.6: Dissolution process relating PTFE volume fraction and mass lost.

The CsH_2PO_4-PTFE composite could only with stand the dissolution process for the first three hours with 30 wt% PTFE volume fraction losing approximately 12 wt% of its mass. The 45 wt% PTFE composite only lost 7 wt% of its mass with the first two hours. The composite with the 50 wt% PTFE performed the best with only 4 wt% lost within the first two hours. A possible explanation could be that the resulting composites produced the salt at the surface and the bulk of the insulator was towards the centre of the composite. With 50 wt% as the salt component, approximately 18 wt% was exposed to the surface.

At temperatures raised to 95 ^{o}C, the higher volume fraction PTFE composites once again required more vigorous conditions to completely dissolve. The higher volume fraction composites, 50 wt% PTFE, lost 20 wt% and 28 wt% for the composites containing 45 wt% PTFE. PTFE weight content of less the 65 wt% experienced rapid dissolution at 95 ^{o}C.

6.4.2 pH determination in relation to the time required for the solubility of the salt in the composite to reach a state where the pH of the solution is affected is recorded here. The performance is relative to the volume fraction PTFE. For the graph below membrane I, J, K and L have volume fractions 0,5; 0,43; 0,35 and 0,30 respectively.

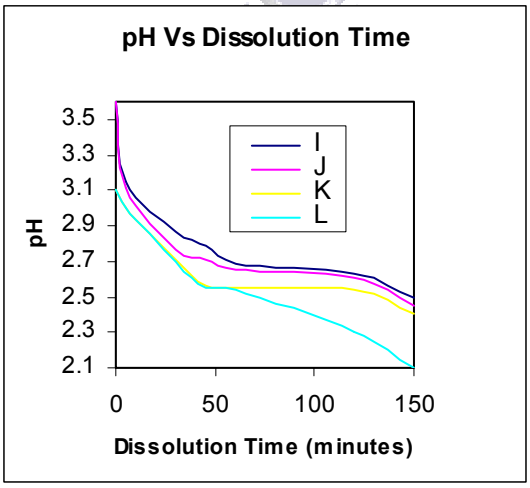

Figure 6.7: Dissolution time relative to pH for CsH_2PO_4 containing composites.

The favourable influence of the PTFE is most pronounced at the higher concentrations of 50 and 43 wt%. This is further influenced by the low room temperature (25°C) that was increased after 20 minutes to 40°C. With an increase in temperature and constant stirring at 300 RMS, a gradual drop in pH was noted with the composites concerned. The effect of temperature, mechanical treatment by stirring and duration of membrane exposure to the environmental conditions, are all factors that influence the stability of

the membrane. Although water is the most significant factor affecting the membrane stability there are secondary influences present in the operational environment of the fuel cell. The heat treatment, in combination with stirring is more effective at destroying the surface and etching away the salt from the composite. A fairly considerable increase in the acidity of the solution was observed which further increased as the stirring rate increased.

6.5 CONDUCTIVITY ANALYSIS

Due to the unstable nature of CsH_2PO_4 proton salt at room temperature, which has the hygroscopic tendency and instant collapse of structure once in contact with moisture, the conductivity could not be measured. Also the required temperature for the super-ionic phase to be reached at around 230°C was not possible with the equipment at the institute. Data from literature to support the use of composites incorporating silica to enhance conductivity is reviewed here.

6.5.1 Conductivity Analysis of Polycrystalline CsH_2PO_4

Typical impedance plots for CsH_2PO_4 pellets were allowed to reach a steady state in a gaseous 30% H_2O/Ar mixture. Semicircles (refer to fig. 5.15) in the low temperature region between 150 and 220°C were present. The semicircles (refer to fig. 5.15) became smaller as the temperature was increased. From this data an equivalent circuit could be established including the parallel combination of a resistance *R* with a CPE where the impedance is

$$Z_Q(\omega)=1/Q(i\omega)^n$$

where Q and n are frequency independent parameters, and i and ω are representative of imaginary unit and angular frequency, respectively. *R*, the resistance is analogous with proton conductivity [64]. The conductivity, σ, was calculated from *R* and pellet

(solid acid electrolyte) dimensions as $\sigma = L/SR$, where L and S are thickness of the pellet and electrode surface area respectively. The complex impedance became small in the temperature region 220-250 ^{o}C. There was an absence of semicircles (refer to fig. 5.15) due to the fast ionic conduction process that the instrument used at the time could not process [6]. The low frequency process, $Z\acute{\imath}(\omega)$ in relation to the impedance of the electrode-electrolyte interface [2] was reflected. Due to equipment limitations, the resistance R for the high temperature region was determined from the extrapolation of $Z\acute{\imath}(\omega)$ to a real axis in the complex plane.

6.5.2 CsH_2PO_4-SiO_2 composites

The conductivities of CsH_2PO_4 / SiO_2 composites were analysed in 30 mol% H_2O in argon balance at atmospheric pressure. This was done, as CsH_2PO_4 is stable under those conditions. Different types of silica were employed in the composites, namely S1, S2 and S3. The resulting impedance spectra of CsH_2PO_4/S1 and CsH_2PO_4/S2 composites reflected two semicircles (refer to fig. 5.15) per impedance plot. The impedance plot of the pure CsH_2PO_4 showed one semicircle (refer to fig. 5.15). When the volume fraction of the silica type (S3) in the CsH_2PO_4/SiO_2 composite was 0.5 there appeared two semicircles and at 0.33 only one semicircle appeared. Thus, it is very important to observe that the shapes of the impedance spectra are dependant on the type of silica used. Similar impedance spectra were obtained in the low temperature region between 150 and 220 ^{o}C. As for the pure CsH_2PO_4 the equipment was not able to display semicircles as the proton conduction at temperatures above 230 ^{o}C was too rapid for the equipment to detect. When silica types S1 and S2 were used with volume fractions of 0.33, the conductivities in the high conductive phase 250 ^{o}C and the low conductive phase at 150°C, decreased by one order of magnitude simultaneously. At temperatures just below the high conductivity phase transition of

220 ^{o}C, the conductivity of composites containing S1 type silica is five times greater than that of S2 type silica containing composites. This is an important observation where the hydrophilicity (silanol groups) of the SiO_2 surface robustly influences the conductivity. For the volume fraction of silica at 0,33 of S3 type silica that has a hydrophilic feature like S1 type silica and a large surface area, the conductivity in the low conductive phase exceeded that of S1 and S2 silica types. But in the high conductive phase the conductivity was similar to that of pure CsH_2PO_4. Another significant observation about the importance of the specific surface area the conductivity of the composite containing silica type S3 volume fraction 0,33 was higher than composites containing silica types S1 and S2 and pure CsH_2PO_4.

Infrared: This is evident in the Si (111) and Si (100) surfaces. Here inelastic tunneling produces multiple vibrational excitations and Si-H bond breaking. The Si-H bond anharmonicity tends to localize the vibrational energy to a single Si-H bond by inhibiting the lateral spreading of the vibrational energy increasing the opportunity for bond breaking.

6.5.3 Factors affecting Conductivity

As for $CsHSO_4$, water content in CsH_2PO_4 is the most significant factor, as the temperature dependent conductivity is affected favourably at low temperatures and possibly again at temperatures above 150 ^{o}C. TGA analysis performed on the composites of varying PTFE content with the intent of displacing the solvent and producing a composite that encouraged the use of a mechanism for proton conduction that is free of water.

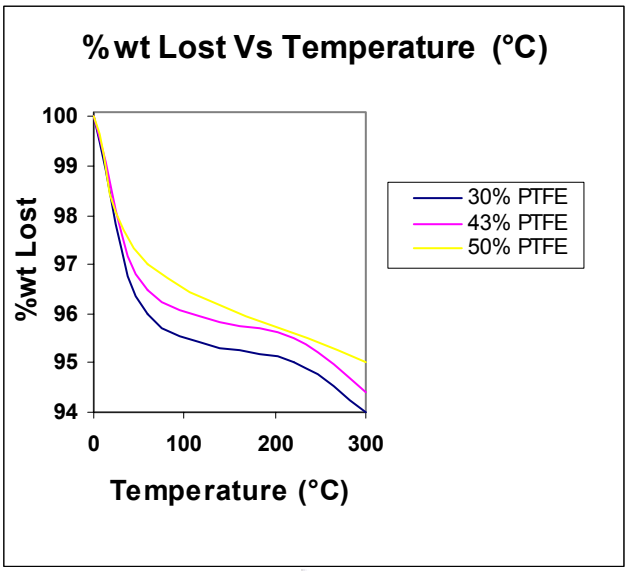

Figure 6.8: TGA of varying CsH_2PO_4 and PTFE volume fractions in composites

The high water content in the CsH_2PO_4 composites is obvious with the immediate loss in weight upon heating although the temperature is in the region of 60 ^oC (333K). The high PTFE content composites do not release water or do not have high water content as the composites with lower PTFE content. These results are consistent with stability test results where the insulator prevents water absorption and does not decompose as easily. Introducing large volume fraction insulator reduces the conductivity capacity of the composite. This would be evident in the general effective media and type of percolation phenomenon with respect to particle size and shape distribution. The conductivity that is thermally dependent for CsH_2PO_4 increases in the temperature region 220 ^oC (493K). This is also the region for the second loss in mass with the majority of the water having moved out of the membrane.

As for $CsHSO_4$ composites there is an increase in conductivity (σ) as the volume fraction of the conducting phase (ϕ) increases as with typical percolation systems for the CsH_2PO_4 composites. A noteworthy increase in conductivity in the region signifying the critical percolation threshold ϕ_c had been reached with gradual increase in conductivity until ϕ=1. For high temperature conductivity and in general, the ϕ_c lies between 0-0.20 (0-20% conductive phase $CsHSO_4$) for CsH_2PO_4 [53]. A composite exceeding the accepted critical volume fraction, which ensures percolation ($\phi > \phi_c$) is equated as

$$\sigma_m = \sigma_c \, [(\phi - \phi_c)/(1 - \phi_c)]^t \qquad [\phi > \phi_c]$$

where, σ_m is the measured conductivity ($S.cm^{-1}$); σ_c is the conductivity of the conductive phase ($S.cm^{-1}$) and t is the percolation exponent. Whether or not there is polychromatic percolation with more than two species occupying the lattice sites, a continuum is observed above 20% volume fraction of the conducting phase. Depending on the shape of the conducting particle the average number of contacts per grain is 1.5 [54]. This would be applicable to the data recorded here as SEM indicates particles are in contact with its neighboring agglomeration of conducting particles. SEM images depicting amorphous composites with granular agglomerations of SiO_2 together with PTFE having insulator properties partially encapsulating the conducting $CsHSO_4$ phase, is 20% insulator by volume fraction. Where the probability of percolation is in the confidence interval and continuous pathways for ion conduction are evident, the t values should be in the region of the universally accepted range. With the ion-conducting phase at 80% of the total composition (i.e. volume fraction 0.8), the calculated t value is 2.4 and the conductivity of the $CsHSO_4$ is 10^{-2} S/cm. In this case of universal contact between the conducting particles the minimum amount or volume fraction to ensure percolation as critical for $CsHSO_4$ was calculated at 0.4.

The lack of continuous paths for the ion conduction was not significant as the conducting phase was always in excess of 50% in the composites.

The conductivity of the composite media can in principle be explained and incorporated in principle by Bruggeman's symmetric, asymmetric and media equations. In the case of the higher volume fraction composites, containing CsH_2PO_4, the conducting phase completely surrounds and encapsulates the other and at most times shows a mono-phase present in the SEM images. The SEM images also depict the intermediate media with two phases visible. This type of composite media can be explained as follows.

$\sigma_m = \sigma_h (1- f/f_c)^t$

Where σ_m is the conductivity of the medium, σ_h is the conductivity of the high conducting phase, f is the volume fraction of the high conducting phase and f_c is the critical volume fraction for the high conducting phase.

This occurs when $\sigma_l = 0$ where σ_l is the conductivity for the low conducting phase which is PTFE. The McLachlan [85, 86] equation proposed above has the mathematical form of a typical percolation equation but is reduced to the Bruggeman symmetric form when $f_c = 1-L_f$ and asymmetric form when $f_c = 1$, where this type of concentration and asymmetric form were not reached as the conducting phase CsH_2PO_4 was in excess of 50 wt% and insulating phase PTFE was as low as 0,3 volume composition fraction. This is true where f_c represents the critical volume fraction of the poor conducting phase ($1-\sigma_c$). Previously determined, the f_c for the high conducting phase was approximately 0,4, resulting in 0,6 as the critical volume fraction for insulating phase, PTFE. For the medium with non-existent resistance with respect to the high conducting phase

$P_m = P_h (1-\phi/\phi_c)^{\phi c/Lc}$

Where P_m refers to the resistance of the composite and P_h to the resistance of the low conducting phase there is a direct relationship with the volume fraction of the high conducting phase being reduced and affected by the critical volume fraction of CsH_2PO_4 as the high conducting phase. The thermal dependent optimum conduction begins to take effect at approximately 220°C (493K) where the phase transition to ion-conductor occurs, here the medium changes with insulator accommodating the structural and chemical changes the CsH_2PO_4 undergoes. As the temperature is raised, the medium could possibly tend towards an asymmetric medium conductor host, where the conductivity of the low conducting phase is significantly reduced and eventually becomes non-existent. This mechanism is proposed as the PTFE particles move away from each other in an attempt to allow the temperature affected or heated conducting salt, to form continuous pathways unlike a symmetric medium. This would explain the agglomerations in the composites toward the periphery of the composite membrane. The symmetric medium with the proportionate arrangement of insulator and conducting substances where $\sigma_l = 0$: $\sigma_m = \sigma_h[1-(3/2)f]$: $f_c = 1-L_f$ and t = 1.

For the symmetric medium, the resistance of the low resistance phase would be close to zero or non-existent i.e. $P_l = 0$; $P_m=P_h(1-3\phi)$; and t=1. At temperatures below the phase transition temperature volume fractions in the region of 0,5 for each the components of the membrane could result in the production of a symmetrically orientated dispersion resulting in exponential t values in the region equal to 1. The critical volume fraction of the high conducting phase, CsH_2PO_4, could be similar to the demagnetization or depolarization coefficient otherwise used to characterize this conducting phase, $\phi_c=L_\phi$.

The media reaches an idealized state where the Bruggeman's symmetric theory could be applied. The temperature changes from below the phase transition to and above the phase transition for that of $CsHSO_4$ and CsH_2PO_4 for the composites with higher amounts conductive material content, will not be affected by the symmetry of the distribution of insulator and conducting material since the conducting paths were present at low temperatures due the high ratios of conducting material in excess of 50 wt% for each composite. Generally $P_m=P_h(1-\phi/\phi_c)^t$ is applicable to the study of composites here, and with the media conductivity of 10^{-2} $S.cm^{-1}$ at approximately 180°C (453K) the percolation in this form can be reduced to Bruggeman's symmetric and asymmetric media formation and the critical limit for the appropriate values of the parameters. The quantification of the parameters including the number of contact sites, the shape and particle size of the proton-conducting material are related by critical parameters for bond site percolation as lattice structure varies with temperature changes. The $CsHSO_4$ and CsH_2PO_4 undergo crystal lattice changes as the temperature is increased and the phase transition is reached and exceeded. Lattice structures include face-centered cubic, body-centered (bcc) and simple cubic (sc). TGA (Thermal gravimetric analysis) data show crystallographic low temperature lattice structures of, simple cubic structures that are usually associated with water content and as heat is applied in the region of 60°C water losses occur as thermal analysis is continued. Data suggesting different types of crystal structure for $CsHSO_4$ and CsH_2PO_4 after phase transition include monoclinic to tetragonal and monoclinic to cubic respectively [6, 53]. Simple cubic critical bond and site probability values are 0,247 and 0,311 respectively. The corresponding volume fraction of the conducting material is calculated as 0,163 where the product of the filling factor and critical site probability is equivalent to the critical volume fraction. For (CsH_2PO_4)

the critical site probability is 0,245 for the body-centered cubic lattice at temperatures in the region 230°C (503K) and critical bond probability 0,179 for similar temperatures. This crystal lattice structure is maintained above the phase transition temperature. The frequency response results indicate the increase in conductivity and smooth graphical representation (Arrehnius representation) upon cooling possibly due to crystal orientation of the site and bond after the loss of water and lack of re-adsorption thereof. Once the crystal structure had been formed due the site probability, the remainder of the composite lattice is filled with insulator PTFE as matrix. On average, the critical volume fraction is in the region 0,16 ± 0,02 for cubic structures of typically high conductive phases, therefore membrane A with 0,8 volume fraction $CsHSO_4$ as solid electrolyte material has the higher probability of forming stable simple cubic lattice structures. This probability of formation decreases as the concentration of electrolyte decreases.

CHAPTER 7

CHAPTER 7 - SUMMARY

The CsH_2PO_4 has proved to be very hygroscopic under test conditions. The pure salt adsorbs water from the atmosphere at room temperature within an hour of exposure. This is further compounded by the formation of water droplets at the surface which, after a short period is absorbed into the membrane, completely softening it and eventually becoming a paste. With the introduction of PTFE here was an improvement in structure stability and mechanical strength. The austerity and stability testing indicated the adverse effect of typical environmental conditions the membrane would encounter during the fuel functioning. High volume fraction PTFE content membranes fare much better than those with less of the stable polymer in its structural framework. When membranes are stored at temperatures above 80 ^{o}C (353K) there is an improvement in performance with respect to the low water content due to the resistance to absorption of water that is greatly enhanced by the PTFE content. These storage conditions are not always practical, as the cost would be adversely affected. The CsH_2PO_4 becomes a superionic conductor when in combination with silica. Silica with varying pore diameter sizes affects the conductivity of the composite favorably by lowering the temperature for phase change and increasing the conductivity considerably. Conductivity above 10^{-2} S/cm in the temperature region of 230-235 ^{o}C was recorded with and without PTFE.

The $CsHSO_4$ salt that is not as hygroscopic as CsH_2PO_4, improved its water resistant properties with the addition of PTFE. This was achieved with insulator concentrations as low as 0.17 volume fraction of the composite and 0,13 silica volume fraction. The superionic phase transition was attained at approximately 132 ^{o}C once silica previously preheated to 900 ^{o}C (1173K) was included in the composition whereas without silica the

phase transition temperature was recorded at approximately 140 ^{o}C. Conductivity in the superionic phase recorded at 10^{-2} S/cm similar to that of the pure salt. Further improvement in the membrane stability with respect to water was noted at higher PTFE volume fractions where water was effectively prevented from being reabsorbed after heating. Stability testing showed that $CsHSO_4$ membranes with higher PTFE content were able to maintain a constant mass for five days unprotected from exposure to the atmosphere. The pH of the test solution did not drop as rapidly in the composites when compared to the pure salt. The acidity of the test solution gives an indication of immiscibility and mechanical strength improvement of the membrane. Infrared analysis revealed the structural resistance to damage when heated to temperatures as high as 170 ^{o}C (443K). High temperature treated composites gave spectra with more defined peaks. This was possibly due to the water loss after 100 ^{o}C (373K) and further removal of solvents that improved the resolution.

Future research and development will be conducted using different group 1 and 2 metals (Periodic Table) inplace of cesium for the composite formations. IR and Raman spectroscopic studies will be used to determine the reversible phase transitions and corresponding temperatures. Conductivity analysis will be performed and compared to that of cesium containing composites. The use of different group 1 and 2 metals could possibly produce a stable solid electrolyte that is less soluble than previously manufactured membranes containing cesium. An in-depth study to compare the particle size distribution and uniformity of the composites with respect to conducting and insulating materials will be performed.

REFERENCES

[1] C. Yang, Journal of Power Sources, 103, 2001 pg.1-9.

[2] M. Casciola, U. Constantino, Solid State Ionics, 20, 1986, pg. 69-73.

[3] M. Casciola, F. Marmottini, A. Peraio, Solid State Ionics, 61, 1993, pg.125-129.

[4] P. Costamagna, C. Yang, A.B. Bocarsly, S. Srinivasan, Electrochimica Acta, 47, 2002, pg. 1023-1033.

[5] E.A. Ticianelli, C.R. Derouin, A. Redondo, S. Srinivasan, Methods to advance technology of proton exchange membrane fuel cells, Journal of Electrochemical Society, 135(9), 1988, pg.2209.

[6] Junichiro Otomo, Naohisa Minagawa, Ching-ju Wen, K. Eguchi, H. Takahashi, Protonic conduction of CsH_2PO_4 and its composite with silica in dry and humid Atmospheres, Solid State Ionics, 156, 2003, pg.357-369.

[7] E. Ortiz, R.A. Vargas, B.E. Mellander, J. Chem. Phys. 110, 10, 1999, pg. 4847

[8] J. Maier, J. Phys. Chem. Solids, 46 (3), 1985, pg.309.

[9] T. Ishii, J. Kawamura, J. Phys. Soc. Jpn., 67 (10), 1998, pg. 3517.

[10] M.G. Lazarraga, J. Ibanez, M. Tabellout, J.M. Rojo, Composite Science and Technology, 64, 2004, pg. 759-765.

[11] S.M. Haile, Solid State Ionics and Electroceramics Research Group, Improved solid acid electrolyte at Caltech, Materials Science Department, Pasedena, California, USA, 2004.

[12] Ph. Colomban, M. Pham-Thi, A. Novak, Solid Sate Ionics, 24, 1987, pg. 193-203.

[13] K. Itoh, T. Ozaki, E. Nakamura, International Union of Chrystallography, 37B, 1981, pg. 1908-1909.

[14] H. Matsunaga, K. Itoh, E. Nakamura, Journal of the Physics Society in Japan,

48, 1980, pg. 2011-2014.

[15] Ph. Colomban, A. Novak, Journal of Molecular Structure, 177, 1988, pg. 277-308.

[16] S. Yokota, Journal of the Physics Society in Japan, 51, 1982, pg.1884.

[17] M. Pham-Thi, Ph. Colomban, A. Novak and R. Blink, Solid State Communcations, 55, 1985, pg. 265.

[18] M. Pham-Thi, Ph. Colomban, A. Novak and R. Blink, Journal of Raman Spectroscopy, 18, 1987, pg. 185.

[19] A. Goypiron, J. de Villepin and A. Novak, Journal of Raman Spectroscopy, 9, 1980, pg. 297.

[20] L. Borjesson and L.M. Torell, Physics Review, 32, 1985, pg. 2471

[21] Ph. Colomban, M. Pham-Thi and A. Novak, Solid State Ionics, 21, 1986, pg.125

[22] D. Semmingsen, W.D. Ellenson, B.C. Frazer and G. Shirane, Physics Review Letter, 38, 1977, pg. 1299.

[23] Ph. Colomban, J.C. Lassegues, A. Novak, M. Pharm-Thi and C. Poisignon, Journal of Lascombe (Ed.), Dynamics of Molecular crystals, 1987, pg. 269.

[24] N.G. Hainovsky, Izvest Sibir Otd. ANSSSR, Ser. Khim. Nauk, 5,1984, pg. 27.

[25] N.G. Hainovsky, and F.F. Hairetdinov, Izvest Sibir Otd. ANSSSR, Ser. Khim. Nauk., 8, 1985, pg. 33.

[26] A.I. Baranov, R.M. Fedosyuk, N.M. Shchagina and L.A. Shuvalov, Ferroelectric Letter, 2, 1984, pg. 25.

[27] M. Komukae, T. Osaka, Y. Makita, T. Ozaki, K. Itoh and E. Nakamura, Journal of the Physics Society in Japan, 50, 1981, pg. 3187.

[28] D.S. McLachlan, M. Blaskiewicz, and R.E. Newman, Journal of the American Ceramic Society, 73 (8), 1990, pg. 2187-2203.

[29] S. M. Ahroni, "Electrical Resistivity of a Composite of Conducting Particles in in an insulating Matrix," Journal of Applied Physics, 43, 1972, pg. 2463-2465.

[30] V.G. Ponomareva, N.F. Uvarov, G.V. Lavrova and E.F. Hairetdinov, Composite Protonic Solid Electrolytes in the $CsHSO_4$-SiO_2 System, Solid State Ionics, 90, 1996, pg. 161-166.

[31] N.F. Uvarov, V.P. Isopov, V. Sharma and A.K. Shukla, Solid State Ionics, 51, 1992, pg. 41.

[32] S. Kirkpatrick, Physics Review Letter, 27, 1971, pg. 1971.

[33] M. Friesel, A. Lunden and B. Baranowski, Solid State Ionics, 35, 1989, pg. 91.

[34] D.A. Skoog, D.M West and F.J Holler, Fundamentals of Analytical Chemistry, 6th edition, 1992, pg. 758-759.

[35] P.H. Bottelberghs, Low Frequency Measurements on Solid Electrolytes and their interpretations, in: Solid Electrolytes, eds. P. Hagenmuller and W. van Gool (Academic Press, New York), 1978, pg. 145-172.

[36] J.R. Macdonald J.A. Garber, Journal of the Electrochemical Society, 124, 1977, pg. 1022.

[37] I.D. Raistrick and R.A. Huggins, Proc. Symposium and Workshop in Advanced Battery Research and Design, 277B, 1976, pg. 76-78.

[38] J.R. Macdonald, Electrode Processes in Solid State Ionics, 1976, pg. 149.

[39] D.R. Franchetti, J. Schooman and J.R. Macdonald, Solid State Ionics, 5, 1981, pg. 617.

[40] B.A. Boukamp and G.A. Wiegers, Solid State Ionics, 9-10, 1983, pg. 1193.

[41] P.H. Bottleberghs and G.H.J. Broers, Journal of Electroanalytical Chemistry, 67, 1976, pg. 155.

[42] I.D. Raistrick, C. Ho and R.A. Huggins, Journal of the Electrochemical Society, 123, 1976, pg. 1469.

[43] J.R. Macdonald, Solid State Ionics, 13, 1984, pg. 147.

[44] J.R. Macdonald, A. Hooper and A.P. Lehnen, Solid State Ionics, 6, 1982, pg. 65.

[45] J.R. Macdonald, J. Schooman and A.P. Lehnen, Journal of Electro-analytical Chemistry, 131, 1982, pg. 77.

[46] B.A. Boukamp and R.A. Huggins, Materials Research Bulletin, 13, 1978, pg. 23.

[47] N.F. Uvarov, E.F. Hairetdinov and N.B. Bratel, Russian Journal of Electrochemistry, 29, 1993, pg. 1406.

[48] N.F. Uvarov, B.B. Bohonov, V.P. Isupov and E.F. Hairetdinov, Solid State Ionics, 74, 1995, pg. 15.

[49] L.J. Bass, G.L. Turner, Anion Distributions in Sodium Silicate Solutions Characterization by NMR and Infrared Spectroscopy and Vapour Phase Osmometry, Journal of Physical Chemistry, 101, 1997, pg. 10641 – 10637.

[50] I. Kiricsi, C. Flego, G. Pazzuconi, W.O. Parker Jr, R. Millini, C. Perego, and G. Bellusi, Journal of Physical Chemistry, 98, 1994, pg. 4627.

[51] J.J. Sumner, S.E. Creager, J.J. Ma and D.D. Mateau, Journal of the Electrochemical Society, 145, 1998, pg. 107.

[52] R.T.C. Slade, A. Hardwick, and P.G. Dickens, Solid State Ionics, 9and10, 1983, pg.1093.

[53] D.A. Boysen, C.R.I. Chisholm, S.M. Haile and S.R. Narayanan, Polymer Solid Acid Membranes Fuel Cell Applications, Journal of the Electrochemical Chemical Society, 147, 2000, pg. 3610-3613.

[54] J. Gurland, An Estimate of Contact and Continuity of Dispersions in Opaque Samples, Transition Metallic Society, 236, 1966, pg. 642-646.

[55] S.M. Haile, G. Lentz, K.D. Kreuer and J. Maier, Superprotonic Conductivity in $Cs_3(HSO_4)_2(H_2PO_4)$, Solid State Ionics, 77, 1995, pg. 128-134.

[56] B. Baranowski, M. Friesel and A. Lunden, Physica, 156A, 1989, pg. 353.

[57] K. Itoh, T. Ukeda, T. Ozaki and E. Nakamura, Acta Cryst., 46C, 1990, pg. 358.

[58] A.V. Belushkin, W.I.F. David, R.M. Ibberson and L.A. Shuvalov, Acta Cryst., 47B, 1991, pg. 161.

[59] V.G. Ponomareva, G.V. Lavrova and L.G. Siminova, The Influence of Heterogeneous Dopant Porous Structure on the Properties of Protonic Solid Electrolyte in the $CsHSO_4 – SiO_2$ System, Solid State Ionics, 118, 1999, pg. 317-323.

[60] J. Maier, Solid State Chemistry, 23, 1995, pg. 171.

[61] C.C. Liang, Journal of the Electrochemical Society, 120, 1973, pg. 1289.

[62] N.G. Dadney, Annual Review of Material Science, 19,1989, pg. 103.

[63] N.F. Uvarov and E.F. Hairetdinov, Solid State Phenomena, 27, 1994, pg. 39-40.

[64] A.I. Baranov, V.P. Khiznichenko, L.A. Shuvalov, Ferrolectrics, 100, 1989, pg.135.

[65] B. Yang, A.M. Kannan, A. Muthiram, Materials Research Bulletin, 38, 2003, pg. 691-698.

[66] A.V. Belushkin, R.L. McGreevy, P. Zetterstrom, L.V. Shuvalov, Physica, 241-243B, 1998, pg. 323-325.

[67] J.A. Rocket and R. Brown, Journal of the Electrochemical Society, 113, 1966 pg. 207.

[68] J.A. Rocket and R. Brown, Journal of the Electrochemical Society, 113, 1966 pg. 865.

[69] S.Srinivasan and H.D. Hurwitz, Electrochim. Acta, 12, 1967, pg. 495.

[70] F.G. Will, Journal of the Electrochemical Society, 110, 1963, pg. 152.

[71] R. Brown and L. Horve, "A Model For Wet-Proofed Porous Electrodes" Electrochemical Spring Society Meeting, 1967.

[72] R.P. Iczkowski, Journal of the Electrochemical Society, 111, 1964, pg. 1078.

[73] K. Kinoshita and J.A.S. Bett, Carbon, 11, 1973, pg. 237.

[74] H. Binder, A. Kohling, K. Richter and G. Sandstede, Electrochim. Acta, 9, 1964, pg. 255.

[75] A.I. Medalia, Journal of Colloid Interface Science, 24, 1967, pg. 393.

[76] A.I. Medalia and F.A. Heckman, Carbon, 7, 1969, pg. 567.

[77] D. Rivin, Rubber Chemical Technology, 1975, pg. 307.

[78] S. Mukerjee, S. Srinivasan and A.J. Appelby, Electrochim. Acta, 38, 1993, pg. 1661.

[79] A. Parthasarathy, B. Dave, S. Srinivasan, A.J. Appelby and C.R. Martin, Journal of the Electrochemical Society, 139, 1992. No pg. Numbers.

[80] B.N. Grgur, N.M. Markovic and P.N. Ross, Can. J. Chem., 75, 1997, pg.1465.

[81] U.A. Paulus, T.J. Schmidt, H.A. Gasteiger and R.J. Behm, Journal of the Electroanalytical Chemistry, 495, 2001, pg. 134.

[82] A. Parathsarathy, C.R. Martin and S. Srinivasan, Journal of the Electrochemical Society, 138, 1991, pg. 916.

[83] M. Peukert, T. Yoneda, R.A. Dalla Betta and M. Boudart, Journal of the Electrochemical Society, 133, 1986, pg. 944.

[84] M.S. Wilson, F.H. Garzon, K.E. Sickafus and S. Gottesfeld, Journal of the Electrochemical Society, 140, 1993. No pg. numbers.

[85] D.S. McLachlan, Equation for the Conductivity of Metal-Insulator Mixtures, Journal of Physics C: Journal of Solid State Physics, C18, 1985, pg. 1891-1897.

[86] D.S. McLachlan, A New Interpretation of Percolation Conductivity Results and Large Critical Regimes, Solid State Communication, 60, 1986, pg. 821-825.